Earth and Planetary Science Letters 458 (2017) 1–13

Contents lists available at ScienceDirect

Earth and Planetary Science Letters

www.elsevier.com/locate/epsl

Evaluating the paleomagnetic potential of single zircon crystals using the Bishop Tuff

Roger R. Fu [a,b,c,*], Benjamin P. Weiss [a], Eduardo A. Lima [a], Pauli Kehayias [d,e], Jefferson F.D.F. Araujo [a], David R. Glenn [d,e], Jeff Gelb [f], Joshua F. Einsle [g], Ann M. Bauer [a], Richard J. Harrison [g], Guleed A.H. Ali [b], Ronald L. Walsworth [d,e]

[a] Department of Earth, Atmospheric and Planetary Sciences, Massachusetts Institute of Technology, Cambridge, MA, USA
[b] Lamont-Doherty Earth Observatory, Columbia University, Palisades, NY, USA
[c] Department of Earth and Planetary Sciences, Harvard University, Cambridge, MA, USA
[d] Harvard-Smithsonian Center for Astrophysics, Cambridge, MA, USA
[e] Department of Physics, Harvard University, Cambridge, MA, USA
[f] Carl Zeiss X-ray Microscopy Inc., Pleasanton, CA, USA
[g] Department of Earth Sciences, University of Cambridge, Cambridge, UK

ARTICLE INFO

Article history:
Received 28 April 2016
Received in revised form 3 August 2016
Accepted 23 September 2016
Available online 2 November 2016
Editor: B. Buffett

Keywords:
paleomagnetism
rock magnetism
zircons
Jack Hills
geodynamo
mineralogy

ABSTRACT

Zircon crystals offer a unique combination of suitability for high-precision radiometric dating and high resistance to alteration. Paleomagnetic experiments on ancient zircons may potentially constrain the history of the earliest geodynamo, which would hold broad implications for the early Earth's interior and atmosphere. However, the ability of zircons to record accurately the geomagnetic field has not been demonstrated. Here we conduct thermal and alternating field (AF) paleointensity experiments on 767.1 thousand year old (ka) zircons from the Bishop Tuff, California. The rapid emplacement of these zircons in a well-characterized magnetic field provides a high-fidelity test of the zircons' intrinsic paleomagnetic recording accuracy. Successful dual heating experiments on eleven zircons measured using a superconducting quantum interference device (SQUID) microscope yield a mean paleointensity of 54.1 ± 6.8 μT (1σ; 42.6 ± 5.3 μT after excluding possible maghemite-bearing zircons), which is consistent with high-precision results from Bishop Tuff whole rock (43.0 ± 3.2 μT). High-resolution quantum diamond magnetic (QDM) mapping, electron microscopy, and X-ray tomography indicate that the bulk of the remanent magnetization in Bishop Tuff zircons is carried by Fe oxides associated with apatite inclusions, which may be susceptible to destruction via metamorphism and aqueous alteration in older zircons. As such, while zircons can reliably record the geomagnetic field, robust zircon-derived paleomagnetic results require careful characterization of the ferromagnetic carrier and demonstration of their occurrence in primary inclusions. We further conclude that a combination of quantum diamond magnetometry and high-resolution imaging can provide detailed, direct characterization of the ferromagnetic mineralogy of geological samples.

1. Introduction

Due to its resistance to metamorphism and weathering processes, the silicate mineral zircon ($ZrSiO_4$) preserves a unique record of the Earth's ancient past. Geochemical studies of zircons routinely provide important constraints on their crystallization environment (e.g., Watson and Harrison, 2005). Moreover, zircons often provide highly accurate radiometric formation ages due to their high initial U to Pb ratio.

Owing in part to these properties, detrital zircon crystals from the Jack Hills of Western Australia are the oldest preserved terrestrial material and have been dated up to 4.37 Ga (Froude et al., 1983; Harrison, 2009; Valley et al., 2014). These zircons provide one of the only known opportunities for direct experimental paleointensity characterization of the earliest geodynamo. Such direct constraints on the Earth's early magnetic field hold key implications for a broad range of geophysical problems. A delayed onset of the geodynamo may imply the persistence of a hot, molten lower mantle or the late initiation of plate tectonics (Labrosse et al., 2007; Nimmo and Stevenson, 2000; O'Neill and Debaille, 2014). On the other hand, an active dynamo during the earliest Hadean eon

* Corresponding author.
E-mail address: rogerfu@fas.harvard.edu (R.R. Fu).

http://dx.doi.org/10.1016/j.epsl.2016.09.038
0012-821X/

may imply an important role for compositionally-driven convection in the core or a magma ocean overturn event (Elkins-Tanton et al., 2005; O'Rourke and Stevenson, 2016). At the same time, the intensity of the geomagnetic field may have exerted strong control on the rate of atmospheric loss (Kulikov et al., 2007).

Previous paleomagnetic experiments on Archean whole rock samples dating suggest the existence of an active geodynamo at 3.5 Ga of possibly lower than modern strength (Biggin et al., 2011; Hale and Dunlop, 1984; Hale, 1987; McElhinny and Senanayake, 1980; Tarduno et al., 2010; Yoshihara and Hamano, 2004). On the other hand, the abundance of nitrogen atoms in lunar soil has been interpreted to suggest the lack of a geodynamo at ∼3.9 Ga (Ozima et al., 2005). Most recently, a paleomagnetic study of Jack Hills zircons proposed that a geodynamo with lower than modern day intensity has existed since ∼4.2 Ga (Tarduno et al., 2015). However, a context study of the Jack Hills area has questioned the likelihood that a primary paleomagnetic record may be retained in Jack Hills zircons, such that the ages of their magnetizations are currently unknown (Weiss et al., 2015).

Despite the potential of zircon paleomagnetism to expand our understanding of the early geodynamo, the ability of single zircon crystals to record accurately ancient magnetic fields has not yet been tested against bulk rock measurements. Zircon is not ferromagnetic and cannot by itself record ambient magnetic fields. Primary Fe oxide inclusions observed in zircon (Timms et al., 2012) can potentially carry remanent magnetization. However, the magnetic recording properties of these and other possible ferromagnetic inclusions in zircon remain largely unknown. Detailed paleomagnetic and rock magnetic characterization of zircon is therefore necessary to establish the validity of any paleomagnetic record retrieved from zircon grains.

A recent rock magnetic characterization of detrital zircons from the Tanzawa tonalitic pluton, Japan, measured the ratios of natural remanent magnetization (NRM) to thermoremanent magnetization (TRM) in 12 zircons and inferred a mean paleointensity of 74 μT, which overestimates paleofields expected for the sample location based on geomagnetic dipole field intensity records (8–31 μT) by a factor of 2 to 9 (Sato et al., 2015). When filtered to include only samples with high TRM acquisition capacities, the mean paleointensity of eight zircons (41 μT) is broadly consistent with actual geomagnetic fields. However, because no physical relationship was established between rock magnetic properties and the accuracy of paleointensities of individual zircons, the filtering criterion used cannot be extended reliably to future paleointensity studies. Furthermore, because the Sato et al. (2015) study only compares mean recorded fields over the span of several million years, it does not resolve whether discrepancies between individual zircon paleointensities and mean field values are due to paleosecular variations or an inability of zircons to record accurately ambient magnetic fields.

A more robust evaluation of zircon's paleomagnetic recording potential therefore requires detailed paleomagnetic experiments on mineralogically well-characterized zircons with simple geologic histories that acquired NRM in a well-constrained magnetic field. At the same time, zircons erupted in ash flows are preferable to deep-sourced plutonic zircons as the latter experienced prolonged cooling histories, which complicates the comparison of recovered paleointensities directly to known geomagnetic field intensities.

The Bishop Tuff is an extensive sequence of rhyolitic ash fall tuffs and ignimbrites in eastern California (Hildreth, 1979; Wilson and Hildreth, 1997). The melts that gave rise to the Bishop Tuff are characterized as evolved silicic magma bodies with high H_2O content (Anderson et al., 1989; Bindeman and Valley, 2002; Wallace et al., 1999). On the basis of inclusion assemblages, trace element concentrations, oxygen isotopic compositions, and Ti-in-zircon thermometry, the Jack Hills zircons are likewise considered to have crystallized from felsic magmas with substantial water content (Hopkins et al., 2010; Mojzsis et al., 2001; Watson and Harrison, 2005; Wilde et al., 2001). The composition of Bishop Tuff zircons may therefore be analogous to that of the Jack Hills samples, although their precise crystallization sequences may have differed given the uncertainties in the crystallization setting of the latter (e.g., Darling et al., 2009; Hopkins et al., 2010; Kemp et al., 2010; Nutman, 2006; Rasmussen et al., 2011). The emplacement of the Bishop Tuff occurred in a period of less than a few years at 767.1 ka, which postdates the Bruhnes–Matuyama reversal (Crowley et al., 2007; Singer et al., 2005; Snow and Yung, 1988; Wilson and Hildreth, 1997). Paleomagnetic records from the deposit were therefore not subject to viscous overprinting in a reversed geomagnetic field or post-depositional metamorphism. Meanwhile, the cooling period of TRM acquisition, likely on the order of tens to a few hundred years (Riehle et al., 1995), was too short to result in internal heterogeneities within the deposit due to paleosecular variation.

A previous paleomagnetic study of the Bishop Tuff showed that densely welded ignimbrite samples contain a primary TRM most likely carried by primary low-Ti titanomagnetite (Gee et al., 2010). Thellier–Thellier paleointensity experiments performed on 89 whole rock samples showed that 52% yielded reliable estimates of the paleomagnetic field intensity. The narrow range of paleointensity values derived from samples recovered from diverse locations and stratigraphic heights (43.0 ± 3.2 μT) confirms that cooling through the temperatures of NRM acquisition occurred sufficiently fast to avoid recording paleosecular variation. Because of the mineralogical properties described above, the simple geologic history, and the availability of detailed characterization of the paleofield intensity during emplacement, Bishop Tuff zircons offer a unique opportunity to evaluate the quality of primary paleomagnetic recording in zircon.

In this study, we conducted thermal and AF paleointensity experiments and characterized the ferromagnetic mineralogy of zircons from the Bishop Tuff. We chose zircons taken from sites adjacent to the locations of samples suggested by Gee et al. (2010) to carry primary TRMs. To acquire paleomagnetic data from single zircons, we developed and describe here novel techniques that permit thermal demagnetization and measurement of samples with starting NRM magnitude as low as 5×10^{-14} A m^2. This sensitivity represents a gain of greater than one order of magnitude for samples subject to thermal demagnetization compared to previous techniques (Fu et al., 2014b; Tarduno et al., 2015). Comparison between single zircon and whole rock thermal paleointensities shows that the two data sets agree to within uncertainty. Results from our magnetic and electron microscopy and X-ray tomography suggest that stable magnetization in Bishop Tuff zircons is carried by Fe-oxides associated with apatite inclusions.

2. Samples and methods

We collected samples from an exposure of the Bishop Tuff from the Owens River Gorge. The sampling location (37.51189°N, 118.57129°W) is approximately 50 m north and 32 m up-section from the base of the ∼150 m thick Gorge Section F (GF) studied by Gee et al. (2010). All of our zircons are therefore found within the dense welded ignimbrite unit Ig1Eb (Wilson and Hildreth, 1997), which oxygen isotopic data indicate experienced limited to no post-depositional hydrothermal alteration (Holt and Taylor, 1998). Assuming that the flow unit was deposited isothermally, its mass density provides an emplacement temperature estimate of ∼660 °C (Gee et al., 2010), although the uncertainty on this temperature estimate is not well-understood. Variations in observed ignimbrite density ∼25 m up-section from our sampling locality may imply non-uniform deposition temperatures; how-

ever, such heterogeneities likely do not significantly affect the assumption of isothermal deposition in the lower part of the Ig1Eb unit where our samples were taken (Wilson and Hildreth, 2003; Riehle et al., 2010). As such, the emplacement temperature implies that our zircons should have recorded a nearly full TRM, although a weaker component of hematite-hosted remanence possibly acquired via chemical alteration may exist at higher unblocking temperatures for some samples (Gee et al., 2010). The close proximity of our samples to the sites used in Gee et al. (2010) implies that the samples experienced similar cooling histories and that a comparison of recovered paleointensities would not require corrections for cooling rate (Yu, 2011). Finally, the location of the samples in a steep-sided canyon minimizes the potential of lightning contamination, which is confirmed by our paleointensity results (see below).

We crushed 2 kg of ignimbrite and separated 40 zircons without the use of a magnetic separator. Isolated zircons, which range between 90 and 180 μm in the longest dimension, were handled using plastic and ceramic tools and kept inside the MIT Paleomagnetism Laboratory class ∼10,000 clean room (DC field <150 nT). We did not apply acid leaching to our zircons, in part because their clear appearance in optical microscopy gave no indication of surface oxides, in contrast to previous reports of brown oxide staining on zircons (Lewis and Senftle, 1966). For AF demagnetization experiments, we measured 15 zircons embedded in EPO-TEK 301 epoxy extruded through a 0.25 μm filter (see Tables 1 and S1 for lists of samples). The surface of this epoxy mount containing the zircons was polished using 1 μm alumina powder. For thermal demagnetization experiments, we embedded 18 zircons in pits drilled into Corning Eagle XG glass slides and secured the zircons using high purity quartz powder (Fig. 1). In both cases, the placement of samples in epoxy or quartz powder insured consistent orientation during the demagnetization process, although the zircons were not oriented in an absolute coordinate system. Our ASC Scientific TD48-SC oven permits temperature reproducibility of ≤5 °C, minimizing discrepancies between NRM and partial TRM (pTRM) heating steps.

Due to the very weak initial NRM moments of zircons (5×10^{-14} to 6×10^{-12} A m^2), we measured all samples using the superconducting quantum interference device (SQUID) microscope in the MIT Paleomagnetism Laboratory (Weiss et al., 2007). For AF demagnetization samples, the polished surface of the epoxy mount was placed in direct contact with the SQUID microscope window, resulting in a sensor-to-sample distance of 180 μm. For thermal demagnetization samples, we placed the SQUID microscope window in contact with the undrilled side of the glass slides, yielding sensor-to-sample separations of ∼230 μm. In both sets of experiments, the SQUID microscope produced magnetic field maps with ∼200 μm spatial resolution. We computed zircon magnetic moments from these magnetic field maps by forward modeling of a dipole magnetic source and optimization of the model dipole parameters so as to match the experimental data. Specifically, we adjusted the three components of the magnetic dipole moment and the spatial location of the source to minimize residuals between the measured magnetic field map and the synthetic field map calculated from the model (for more details, see Fu et al., 2014a and Lima and Weiss, 2016).

The epoxy and glass mounts, when measured without samples, displayed a small number (1–2 per mount) of contaminating magnetic sources with moment 1–7 $\times 10^{-14}$ A m^2. Although the upper end of this range overlaps with the weakest measured zircon moments, SQUID microscopy showed that the location of these sources do not coincide with that of measured zircons and therefore do not affect our computed zircon magnetizations (Fig. 1). At the locations of the mounted zircons in the magnetic field map, temporal fluctuations in the SQUID microscope sensor resulted in noise of up to 50 pT (Fig. 1). Assuming that the signal from a zircon must exceed this field strength to constitute a robust measurement, a zircon must have in this particular configuration (sensor-to-sample separation of 230 μm) a dipole moment of $>6.0 \times 10^{-15}$ A m^2. Because this calculation does not take into account improvements in signal-to-noise ratio from signal processing techniques and the fact that the optimization algorithm can retrieve dipole moments at higher noise levels, the

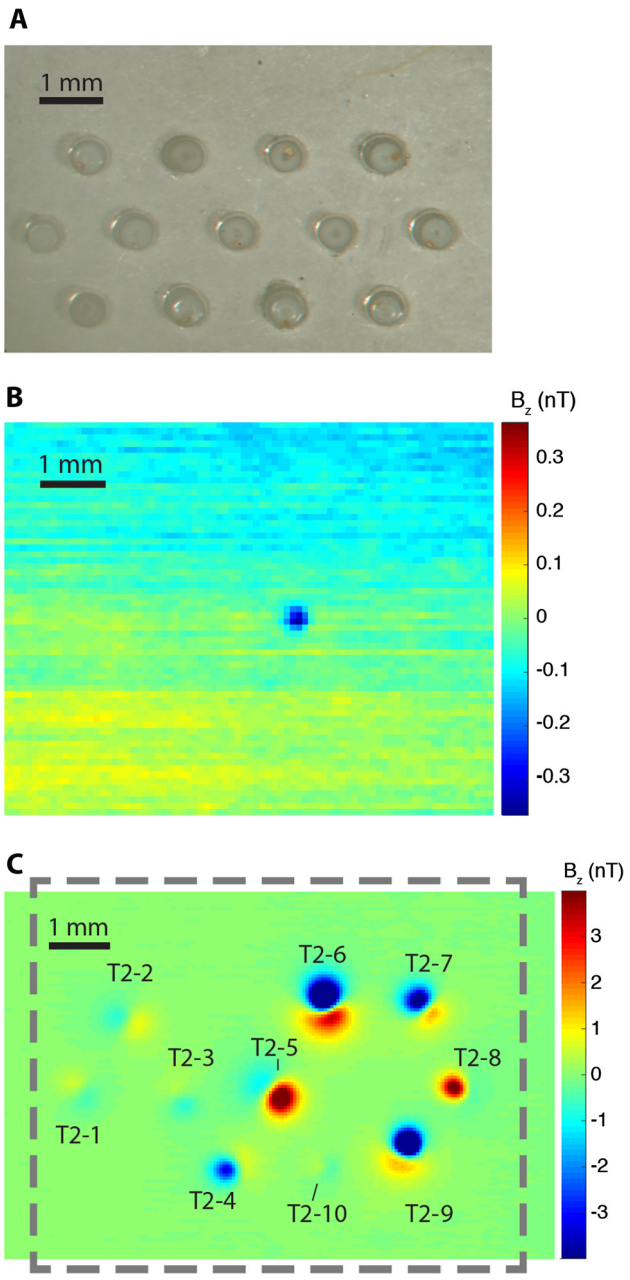

Fig. 1. (**A**) Optical photograph of the glass sample holder with zircons T2-1 through T2-10 mounted inside pits, (**B**) SQUID microscope map of the same sample holder with no zircons, and (**C**) SQUID microscope map of the sample holder with T2 zircons mounted. Shown is the vertical component of the magnetic field at a height of ∼230 μm, with positive (negative) field values representing out-of-plane (into-plane) field directions. The magnetic field signature associated with each zircon is labeled (notice that due to variability in holder fabrication, not every pit was used to house a zircon). Gray dashed box in panel C indicates the area of the map in panel B. Note the different field strength (color) scales between panels B and C. All three panels have the same scale bar. Complete raw data, processed products, and additional documentation of procedures are available in the Supplementary Data. (For interpretation of the references to color in this figure legend, the reader is referred to the web version of this article.)

value of 6.0×10^{-15} A m^2 represents a conservative estimate of our ability to characterize a zircon signal from a raw SQUID microscope map. This limiting moment is higher than that given in previous SQUID microscope-based studies (Fu et al., 2014b; Weiss et al., 2007) due to the higher (230 μm) sensor-to-sample separation necessitated by the thermal demagnetization procedure.

We performed further rock magnetic characterization of selected zircons after their NRMs were removed via AF demagnetization. We used a JEOL 8200 electron microprobe in the MIT Petrology Laboratory set at an accelerating potential of 15 keV to image and characterize ferromagnetic mineralogy. To complement and guide these analyses, we mapped the location of ferromagnetic sources in the zircons using the quantum diamond microscope (QDM) developed at the Walsworth Laboratory at Harvard University. This instrument, which was first used on geological samples to localize ferromagnetism in dusty olivine-bearing chondrules from the Semarkona meteorite (Fu et al., 2014b), produces maps of the magnetic field above a polished sample with a spatial resolution of 2.4 μm and DC noise floor of ∼160 nT. The QDM employs a dense layer of fluorescent quantum magnetic field sensors, nitrogen vacancy color centers, near the surface of a diamond chip on which the sample of interest is placed (Glenn et al., 2015).

Finally, we used the ZEISS Xradia 520 Versa and Ultra XRM-L200 from Xradia, Inc. (now Carl Zeiss X-ray Microscopy) microscopes to obtain tomographic volume reconstructions of a single zircon grain (A7) with 400 nm and 65 nm voxel size, respectively. These voxel sizes give spatial resolutions of 750 nm and 150 nm, respectively, based on measured test patterns using visual inspection and a Modular Transfer Function. We extracted this zircon, which was subjected earlier to AF demagnetization, QDM, and electron microprobe analyses, from the epoxy holder and remounted it onto a ∼50 μm needle tip with superglue for X-ray tomography studies. Both X-ray microscopes were used in absorption contrast mode, in which the contrast roughly scales with mass density.

The sub-micrometer Versa XRM was operated at an accelerating voltage of 60 keV and power of 5 W using the full spectrum of the X-ray beam; the nanoscale Ultra XRM was operated at a quasi-monochromatic X-ray energy of 8 keV, above the Fe absorption edge, which produced a large contrast signal for the Fe oxide particles compared to other materials in the volume studied. For the sub-micrometer-scale Versa XRM imaging, 1601 images were collected at a step size of 0.23 degrees for a total acquisition time of 2 h; for the nanoscale XRM tomographic series, 901 projection radiographs were acquired with an angular resolution of 0.2 degrees and a total scan time of 13 h. After acquisition, the two series of radiographs were aligned and reconstructed using the ZEISS XM-Reconstructor software. Visualization and analysis of the resulting three-dimensional (3D) volumes were performed using ORS Visual Si Advanced and Zeiss XM3DViewer.

3. Results

3.1. Paleomagnetic measurements

We performed thermal demagnetization and paleointensity analysis on 18 zircons whose NRM intensities range between 5.2×10^{-14} and 5.7×10^{-12} A m^2 with a mean of 1.3×10^{-12} A m^2 and median of 9.1×10^{-13} A m^2. For ten zircons composing the T2 group (Tables 1–2), we implemented the IZZI (in-field, zero-field, zero-field, in-field) protocol where samples are heated in a 0 μT and a 50 μT field for each temperature step in alternating order (Yu et al., 2004). We heated samples up to 673 °C in 25 steps, with 10 °C steps between 520 °C and 583 °C and performed pTRM checks at seven temperatures between 269 °C and 583 °C. For eight zircons composing the T1 group, the full thermal demagnetization sequence, which consisted of 20 steps up to 680 °C, was completed before pTRM acquisition experiments in order to acquire demagnetization sequences of the NRM with the least possible amount of sample alteration. The data for these eight zircons therefore did not include pTRM checks. All heating was conducted in air for 30 minutes at the peak temperature, although the isolation of zircons by a ∼1 mm layer of packed quartz powder may have limited chemical exchange with the oven environment.

We used directional demagnetization data (i.e., orthogonal projection diagrams; Figs. 2, S2, S4, S6) to identify the highest fidelity range of demagnetization steps for each zircon for paleointensity calculations. Seventeen out of eighteen zircons subjected to thermal demagnetization carry a resolvable component of magnetization with maximum angle of deviation (MAD) less than 25° (Table 1; Kirschvink, 1980), although directionally coherent magnetization in zircon T2-10 was blocked below only 150 °C. Because the Bishop Tuff was deposited after the Brunhes–Matuyama reversal, we do not observe overprints of reverse polarity in our demagnetization sequences. Even so, lower temperature components with maximum unblocking temperatures below 540 °C are observed in five zircons (T1-5, T1-8, T2-5, T2-7, T2-9; Figs. 2, S2). Because compaction of cooling ignimbrite units may continue down to temperatures <600 °C (Riehle, 1973), these lower temperature components may represent rotation of the zircon during the compaction process.

We compare the MAD and deviation angle (DANG) of the observed components of magnetization to test whether they trend to the origin (Table 1; Tauxe and Staudigel, 2004). For eight out of sixteen zircons used in paleointensity analysis, the value of DANG for the magnetization component chosen for computing paleointensity is less than or approximately equal to the MAD, suggesting that these components are origin-trending. Of the remaining nine zircons, four (T1-1, T1-5, T1-7, and T2-8) carry higher temperature magnetizations. The lower temperature components analyzed for paleointensity in these zircons are therefore not expected to be origin-trending. For a final group of four zircons (T1-2, T1-8, T2-2, and T2-4), noisy demagnetization sequences at higher temperatures may confound the isolation of a higher-temperature component. In any case, only one of these last four zircons (T1-8) passes the quality criteria adopted for computing the mean paleointensity (see below). As such, ten out of eleven zircons ultimately selected to determine the mean paleointensity have their paleointensities determined from either origin-trending magnetizations or carry components at higher temperatures.

In total, eleven zircons have a magnetization component blocked entirely below 580 °C with the majority showing maximum unblocking temperatures between 530 and 580 °C. These components are likely carried by magnetite or titanomagnetite, which is consistent with the findings of Gee et al. (2010). At the same time, eleven zircons have a maximum unblocking temperature above 580 °C, most likely indicating the presence of maghemite or titanohematite (Fig. 3). Gee et al. (2010) observed a high temperature component of magnetization unblocking over the same temperature range and interpreted it as a thermochemical remanent magnetization (TCRM) most likely carried by maghemite, although a primary remanence carried by titanohematite cannot be ruled out. The low maximum coercivities (≤130 mT) of our zircons observed during AF demagnetization argues in favor of maghemite. On the other hand, maghemite usually undergoes inversion to hematite below 600 °C (Dunlop and Ozdemir, 1997). We therefore consider both minerals as a possible carrier for >580 °C remanence in our analysis.

In the scenario that these high temperature components represent a maghemite-carried TCRM, their recovered paleointensities may be biased (Fabian, 2009). At the same time, a primary TRM carried by titanohematite blocked at such temperatures may be af-

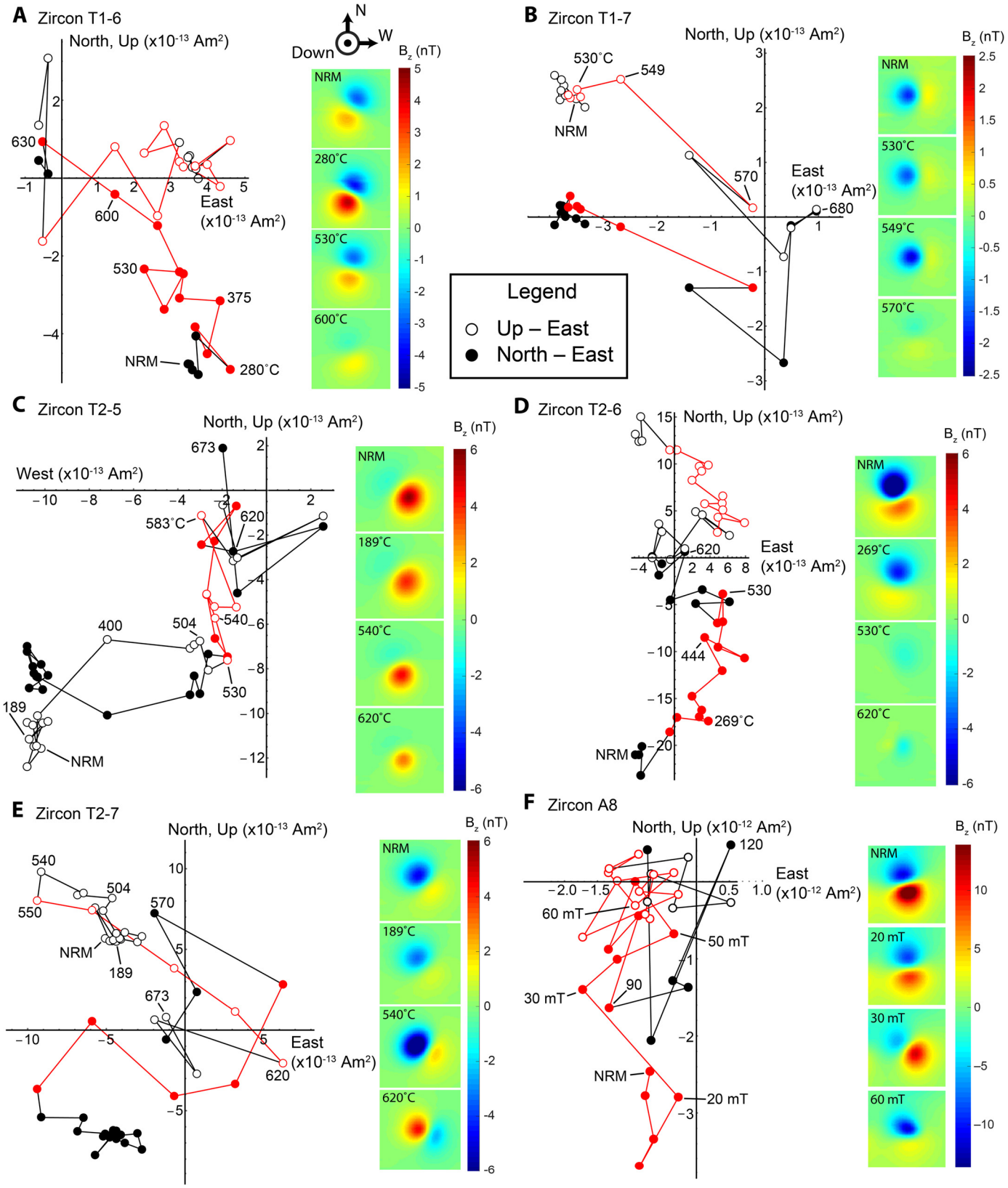

Fig. 2. Orthogonal projection diagrams of single zircon demagnetization. Sequences (**A–E**) show one or two component magnetizations. Panel C shows an example of a high noise demagnetization sequence that was not included in the final paleointensity analysis while panels A, B, D, and E show zircons with higher stability (see Table 1). Typical AF demagnetization sequence (**F**) shows significantly higher noise compared to thermal demagnetization. Solid and open circles denote the projection of magnetization in the horizontal and vertical planes, respectively. Red data points indicate range used in paleointensity calculations. Insets in each panel show the SQUID microscope maps of zircons at the indicated demagnetization steps [shown is the vertical component of the magnetic field at a height of ~230 μm, with positive (negative) field values representing out-of-plane (into-plane) field directions]. Paleointensity (Arai) diagrams for the same six zircons shown here are plotted in Fig. 4. (For interpretation of the references to color in this figure legend, the reader is referred to the web version of this article.)

Table 1
Results of thermal demagnetization experiments on single zircons.

Sample name	Initial NRM ($\times 10^{-12}$ A m^2)	Main component range (°C)	MAD (°)	DANG (°)	Additional component(s) range (°C)	MAD (°)	DANG (°)
T1-1	2.92	504–570	9.0	55.8	600–655	19.1	17.0
T1-2	0.93	375–530	15.2	21.1			
T1-3	5.72	20–530	7.2	7.5			
T1-4	2.29	375-570	18.7	10.0			
T1-5	1.55	305–549	15.9	71.4	549–655	27.8	7.35
					20–280	21.8	78.6
T1-6	0.61	280–630	20.1	11.1			
T1-7	0.39	425–570	10.4	19.4	630–680	8.7	17.0
T1-8	0.88	504–600	15.8	57.2	280–504	13.4	53.0
T2-1	0.18	520–640 (−583)	18.6	14.7			
T2-2	0.46	570–620	13.6	29.4			
T2-3	0.25	None	N/A	N/A			
T2-4	0.61	20–444 (−300)	20.7	48.5			
T2-5	1.73	504–583	24.2	19.6	360–504	17.3	52.4
T2-6	2.52	189–540	19.4	30.0	540–620	38.3	7.4
T2-7	1.00	550–620	17.9	9.8	640–673	30.1	7.6
					360–540	12.6	128.1
T2-8	0.57	20–530	14.0	26.4	560–640	17.1	12.5
T2-9	1.50	504–640	13.3	2.8	20–504	20.3	33.3
T2-10	0.05	None	N/A	N/A	20–150	19.7	6.89

Notes: Only the "main component" of magnetization observed in each zircon (column three) is interpreted as a primary TRM or TCRM and used for paleointensity analysis. Temperature limits for each component are based on the identification of magnetization components from the demagnetization sequence. MAD in columns 4 and 7 refers to the maximum angular deviation, which quantifies the scatter of demagnetization steps around the mean direction. DANG in columns 5 and 8 refers to the deviation angle, which is the angular separation between the best-fit direction of the magnetization component with and without requirement for the fitted line to pass through the origin.

fected by pre-depositional tumbling of the zircons. Therefore, we exclude the highest temperature components of magnetization if they are blocked exclusively >540 °C because a large fraction of these magnetizations may be pre-depositional or due to maghemitization. Such high temperature components of remanence are observed in six zircons (Table 1). For zircon T2-7, we make an exception and perform paleointensity analysis on a component unblocking between 550 and 620 °C because of the presence of an even higher temperature component in a different direction, suggesting that the lower temperature component was not formed in the same maghemitization event or during tumbling if the >620 °C component has such an origin. Besides T2-7, the component selected for paleointensity analysis in three other zircons (T1-6, T2-1, T2-9) unblocks in part above 580 °C, although the lower limit to the component temperature range are below 540 °C.

Applying these considerations for the selection of a component suitable for paleointensity analysis, we computed the paleointensities of sixteen zircons using a linear least-squares fit (Figs. 4, S3, S5, Table 2; Coe et al., 1978). We then evaluated the fidelity of each paleointensity experiment using the normalized error of the best-fit slope ($\sigma/|b|$; Selkin and Tauxe, 2000), the fraction of NRM intensity represented in the fitted data range (f), the gap factor representing the evenness of NRM loss at each demagnetization step (g), and the quality index (q; Coe et al., 1978). Fourteen out of sixteen zircons yielded a value for f greater than 0.5 and a least-squares fit range that includes four or more data points, suggesting that the paleointensities are based on a sufficiently large fraction of the sample magnetizations (Table 2; Coe et al., 1978). On the other hand, zircons displayed a wide range of $\sigma/|b|$ between 0.03 and 0.42. Although paleointensity studies of well-behaved whole rock samples typically adopt a value in the 0.05–0.10 range as the maximum acceptable $\sigma/|b|$ (Gee et al., 2010; Tauxe et al., 2013), the very weak magnetizations of our zircons led to significantly greater scatter compared to high quality whole rock samples. We therefore included all zircons with $\sigma/|b| < 0.25$ in our mean paleointensity calculation. After the application of this quality filter the number of zircons included in the final mean paleointensity calculation was reduced from sixteen to eleven (Table 2). We note that the higher fraction of zircons in the T1 group relative to the T2 group that yields successful paleointensity estimates may be

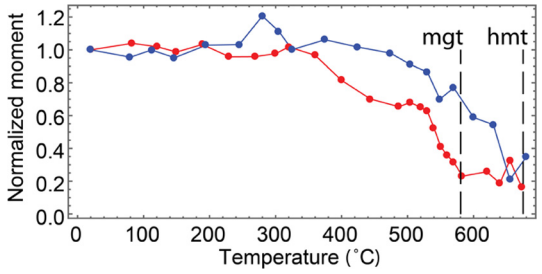

Fig. 3. Moment decay during thermal demagnetization of NRM for two zircons. The dominant ferromagnetic phase in samples T1-8 (blue) and T2-5 (red) are hematite and magnetite, respectively. Dashed lines indicate the Curie temperatures for magnetite (mgt) and hematite (hmt). (For interpretation of the references to color in this figure legend, the reader is referred to the web version of this article.)

attributable to the higher mean moments of these zircons, which leads to lower noise from both measurement and inherent sources. The selection of the T1 zircons prior to T2 samples resulted in, on average, larger zircons that likely caused the higher moments.

For the final group of eleven zircons that pass all reliability criteria above, the mean value for the quality index is 4.28 while the mean MAD is 15.2° with a maximum of 20.1°. These zircons yield a mean paleointensity of 54.1 ± 6.8 μT (1σ of mean), which is statistically indistinguishable ($P = 0.14$) from value of 43.0 ± 3.2 μT derived from 46 higher fidelity bulk Bishop Tuff sample (Fig. 5; Gee et al., 2010). Four zircons in this group have maximum component unblocking temperatures >580 °C, implying that part of the remanence may be a TCRM carried by maghemite and resulting in potentially biased paleointensities. We note that although the nominal highest unblocking temperature in sample T1-8 is 600 °C, the previous heating step was 570 °C. The magnetization in T1-8 may therefore be carried exclusively by magnetite, which is supported by the fact that decay of the component begins at 520 °C. Excluding these zircons yields a mean of 42.6 ± 5.3 μT. The mean paleointensity of the four excluded zircons excluded due to maximum unblocking temperature >580 °C is 74.4 ± 10.6 μT, which may be higher than that of the other zircons ($P = 0.11$) and supports the presence of maghemite (Fabian, 2009).

Although we conducted repeated pTRM acquisition experiments on ten zircons to check for chemical alteration, the inherently

Table 2
Results of dual-heating paleointensity experiments on single zircons.

Sample name	Normalized scatter ($\sigma/\|b\|$)	NRM fraction (f)	Gap factor (g)	Quality index (q)	Number of steps (N)	Paleointensity (μT)	1σ uncertainty (μT)	Included in mean
T1-1	0.14	0.61	0.52	2.29	4	39.4	5.5	Yes
T1-2	0.31	0.53	0.72	1.24	5	59.5	18.5	No
T1-3	0.16	1.14	0.87	6.12	13	59.9	9.7	Yes
T1-4	0.24	1.06	0.55	2.42	7	51.0	12.3	Yes
T1-5	0.17	0.50	0.80	2.29	8	15.9	2.8	Yes
T1-6	0.14	0.95	0.83	5.55	12	50.5	7.2	Yes
T1-7	0.035	0.92	0.44	11.69	6	45.7	1.6	Yes
T1-8	0.24	0.80	0.72	2.37	5	49.3	11.2	Yes
T2-1	0.15	0.57	0.35	1.38	8	63.7	9.3	Yes
T2-2	0.42	0.37	0.41	0.36	3	64.8	27.3	No
T2-3	N/A	N/A	N/A	N/A	N/A	N/A	N/A	No
T2-4	0.26	0.45	0.55	0.93	10	128.5	33.9	No
T2-5	0.39	0.76	0.55	1.06	8	64.1	25.0	No
T2-6	0.14	0.85	0.88	5.18	13	36.9	5.3	Yes
T2-7	0.14	0.89	0.73	4.65	6	86.3	12.1	Yes
T2-8	0.27	0.61	−0.20	−0.45	16	149.6	40.5	No
T2-9	0.14	0.84	0.52	3.12	11	97.0	13.6	Yes
T2-10	N/A	N/A	N/A	N/A	N/A	N/A	N/A	No
Mean						54.1	6.8	

Notes: Only analysis of the main magnetization component of each zircon is shown here. Inclusion in overall mean required $\sigma/|b| \leq 0.25$. See text for details. Column 2 gives the 1σ uncertainty of the best-fit slope in the Arai diagram normalized by the slope value following the method of Coe et al. (1978). Column 3 gives the magnitude of the NRM over which the paleointensity fit is performed as a fraction of the total as defined by Coe et al. (1978). Column 4 and 5 quantify the evenness of spacing between fitted points in the Arai diagram and the overall quality factor, respectively, as defined by Coe et al. (1978). Column 6 gives the number of demagnetization step included in the paleointensity analysis.

Table 3
Summary of pTRM check results.

Sample	ΔpTRM$_{max}$ (10^{-13} A m^2)	ΔpTRM$_{max}/\sigma_{pTRM}$	DRAT$_{max}$	Fit range ΔpTRM$_{max}$ (10^{-13} A m^2)	Fit range ΔpTRM$_{max}/\sigma_{pTRM}$	Fit range DRAT$_{max}$
T2-1	0.79	2.70	0.51	0.38	1.31	0.25
T2-2	7.90	1.80	1.08	7.90	1.80	1.08
T2-3	1.78	1.70	N/A	N/A	N/A	N/A
T2-4	2.52	0.68	1.07	0.59	0.68	0.25
T2-5	4.08	2.04	0.43	4.08	2.04	0.43
T2-6	4.23	0.48	0.26	1.85	0.48	0.11
T2-7	3.23	1.74	0.13	3.23	1.74	0.13
T2-8	1.02	0.79	0.28	1.02	0.79	0.28
T2-9	1.48	1.90	0.12	1.48	1.90	0.12
T2-10	2.94	4.10	N/A	N/A	N/A	N/A

Notes: In column 2, the quantity ΔpTRM$_{max}$ represents the largest difference between repeated pTRM acquisitions at the same temperature for the sample. Column 3 gives the normalized values of ΔpTRM$_{max}$ divided by σ_{pTRM} (the standard deviation of difference between pTRM gained and the best-fit value from the Arai diagram, see text). Column 4 gives the highest absolute value of the DRAT parameter as defined by Selkin and Tauxe (2000). The final three columns show values of each parameter within the temperature range used to fit for paleointensity. For a pTRM check to be included, highest demagnetization step achieved before the pTRM check must fall within the fit range. Zircons T2-3 and T2-10 had no identifiable components on which to compute paleointensity.

large-scatter demagnetization sequences of the weak zircon samples complicate the interpretation of these results (Table 3). In addition to measurement noise, the smaller number of ferromagnetic grains contained in each zircon sample in comparison to a standard ∼2.5 cm paleomagnetic core increases the observed scatter during demagnetization and may result in ∼10% statistical uncertainty in paleointensities derived from zircons with our observed range of NRM moments (Berndt et al., 2016). A standard criterion to evaluate the degree of alteration is the difference ratio (DRAT), which normalizes the difference in the original and repeated pTRMs acquired at a given temperature (ΔpTRM$_{max}$) by the length of the line segment fitted across the temperature range used to compute paleointensity (Selkin and Tauxe, 2000). For well-behaved, whole rock samples, maximum DRAT values greater than 0.05 or 0.10 have typically been adopted as a sign of sample alteration. However, the original DRAT parameter was defined for strongly magnetized samples where the scatter of each measurement is small compared to the change in magnetization between temperature steps. In contrast, the scatter observed in the Arai diagrams for individual zircons is often comparable to the change between temperature steps (Fig. 4). Because the observed value of ΔpTRM$_{max}$ contains contributions from both intrinsic scatter and true change in sample pTRM acquisition due to alteration, the canonical DRAT parameter may significantly overestimate the effect of sample alteration in zircons and other weakly-magnetized samples. As a result, the maximum DRAT parameter calculated for our zircons exceeds 0.10 for all samples.

As an alternative, we computed the quantity σ_{pTRM}, which we define as the standard deviation of the difference between the observed pTRM gained and the best-fit value derived from the Arai diagram (i.e., the x-coordinate difference between data points on the Arai diagram and the best-fit line). Under the assumption that a linear trend exists in the Arai diagram, σ_{pTRM} estimates the amount of variation in pTRM acquisition that is due to measurement noise. We then computed the ratio ΔpTRM$_{max}/\sigma_{pTRM}$ to determine whether the observed value of ΔpTRM$_{max}$ may be attributed to measurement scatter. A value of ΔpTRM$_{max}/\sigma_{pTRM}$ greater than 2 indicates that the observed change in repeated pTRM acquisitions is unlikely (probability $P < 0.05$) to be due to random scatter alone and suggests the onset of sample alteration.

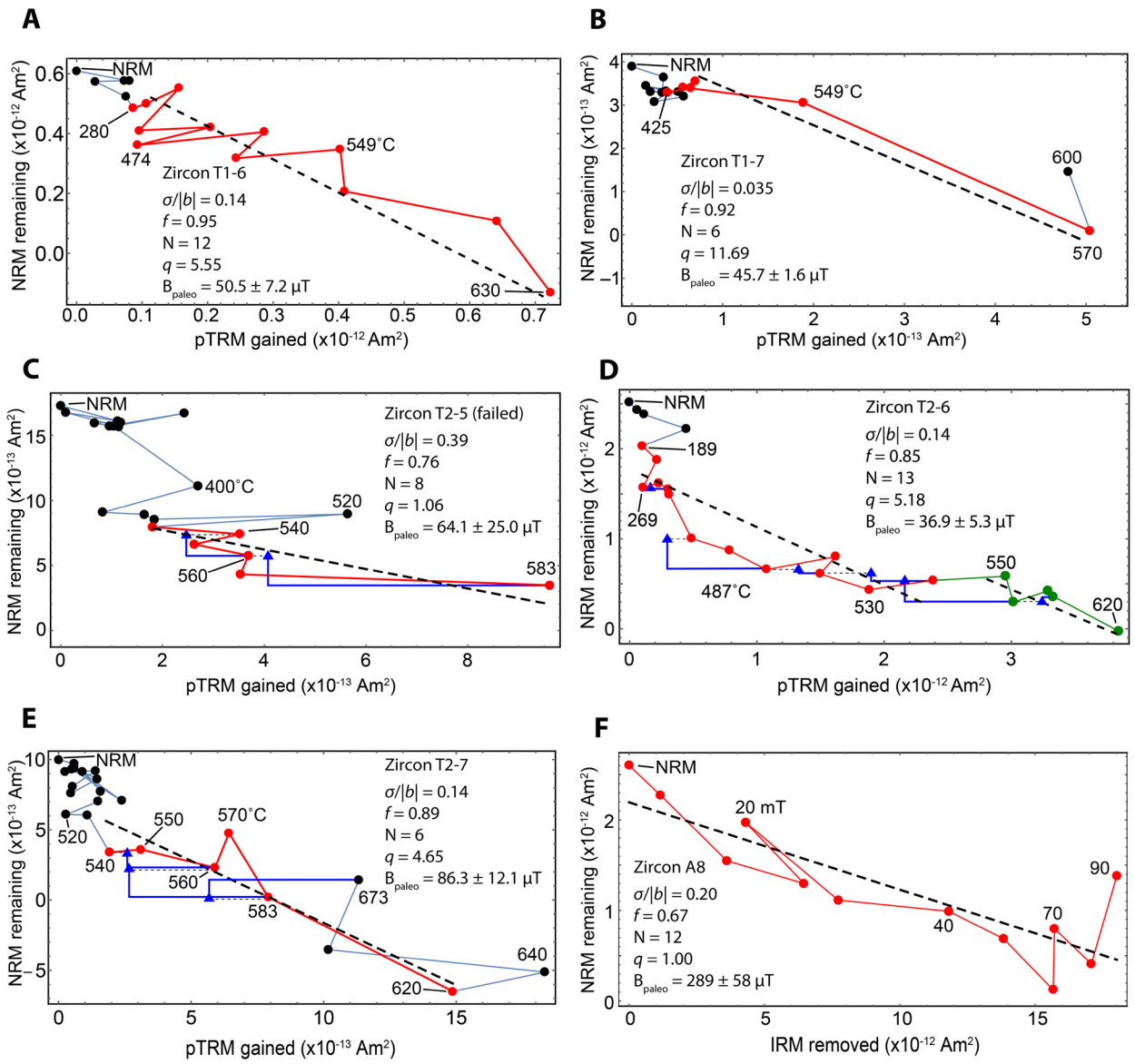

Fig. 4. Paleointensity (Arai) diagrams for zircons subjected to (**A–E**) thermal- and (**F**) AF-based paleointensity analysis. Directional demagnetization data (Zijderveld diagrams) for these four zircons are shown in Fig. 2. Of the thermally analyzed zircons, T1-6 and T1-7 (panels A and B) were treated with sequential thermal demagnetization and pTRM acquisition while T2-5 through T2-7 (panels C-E) were measured using the IZZI Thellier–Thellier protocol including pTRM checks (blue triangles). Panel C shows data typical of zircons not included in the final paleointensity mean due to high scatter. Dashed black lines show the least-squares fit to the chosen data range, indicated in red. The concave up trend seen for some zircons may be indicative of multi-domain (MD) ferromagnetic minerals. (For interpretation of the references to color in this figure legend, the reader is referred to the web version of this article.)

By this criterion, three out of ten zircons experienced significant alteration between 487 °C and 673 °C (Table 3). When considering only pTRM checks within the temperature range used to compute paleointensities, we find that all zircons except T2-5 pass this quality criterion. However, as described above, our simple method of calculating σ_{pTRM} may overestimate pTRM scatter as it does not account for nonlinearity of data points in the Arai diagram. Future studies of similarly weak samples may benefit from performing two or more repeated pTRM acquisition experiments after the same higher temperature step to provide an estimate of the inherent scatter in pTRM measurements.

For AF-treated zircons, we find that, using a typical calibration factor of $a = 3000$ μT the IRM normalization method greatly overestimates paleointensities, yielding a mean paleointensity of 437 ± 95 μT derived from 11 zircons. We provide details for the analysis of AF demagnetization data in the Supplementary Materials.

3.2. Microscopy of Bishop Tuff zircons

After the completion of AF demagnetization and IRM acquisition experiments described above, we applied magnetic and electron microscopy techniques to zircons A1–A15 to characterize their ferromagnetic mineralogy. A key goal is to establish whether the ferromagnetic minerals are concentrated in specific inclusions or dispersed throughout the zircon grain itself. In the latter case, the ferromagnetic minerals may be more resistant to alteration due to the armoring effect of the zircon. Meanwhile, localized inclusions, particularly those at the zircon edges, may be more susceptible to aqueous alteration. We first used the high-resolution magnetic field imaging capability of the QDM to localize the sources of ferromagnetism (Fig. 6). By imparting an out-of-plane IRM of 0.4 T and placing the nitrogen-vacancy-bearing diamond chip against the polished surface of the epoxy mount, we mapped the magnetic field at a sensor-to-sample distance of ~1 μm from the zircon

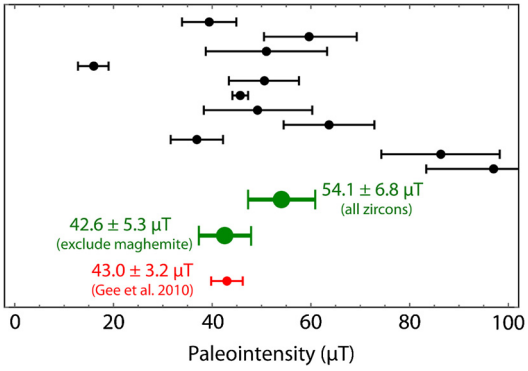

Fig. 5. Paleointensity and 1σ uncertainty for all eleven zircons included in the mean (black). Order from top to bottom corresponds to that shown in Tables 1 and 2. Group means for our zircons with and without possible maghemite-bearing specimens are shown in green while the result of bulk samples from Gee et al. (2010) is shown in red. All uncertainties are 1σ. (For interpretation of the references to color in this figure legend, the reader is referred to the web version of this article.)

surface. Locations with strong out-of-plane magnetic fields indicate the presence of ferromagnetic material at the surface or subsurface. The highly non-uniform spatial distribution of magnetic field sources suggests that ferromagnetic phases are concentrated in inclusions inside the zircon or in uniquely Fe-rich sub-volumes of the zircon grain itself.

These observed distributions of magnetic fields are not consistent with ferromagnetic grains uniformly dispersed throughout the zircon (e.g., Timms et al., 2012), which would result in a spatially broad magnetic field across the full exposed surface of the zircon. We can place an order-of-magnitude upper bound on the contribution to the total paleointensity from hypothetical volumetrically dispersed ferromagnetic sources (which we refer to as the zircon's "dispersed magnetization"). To do this, we selected a zircon (A15) with few localized sources and performed magnetic moment inversions on four localized sources. We then subtracted the dipolar magnetic field associated with each source from the QDM map (Fig. S1A–B; Supplementary Materials). The residual magnetic fields after subtracting contributions from these localized sources should be due to the dispersed magnetization, if any. Fitting the residual field to that expected to be produced by dispersed magnetization yields a moment of 8.7×10^{-14} A m^2, which is weaker than the 2.0×10^{-13} A m^2 moment from the strongest localized source. Because some of this signal may be due to subsurface, localized ferromagnetic sources, we regard 8.7×10^{-14} A m^2 ($\sim$0.2 A/m) as an upper bound to the dispersed magnetization contribution to the IRM. Furthermore, since the expected NRM moments are weaker by a factor of $\sim$7 than the IRM (see Supplementary Materials), the maximum NRM moment contributed by dispersed magnetization is 1.2×10^{-14} A m^2. We therefore conclude that volumetrically dispersed sources in zircon grain A15 contribute at most $\sim$1% of the total moment of typical zircons with

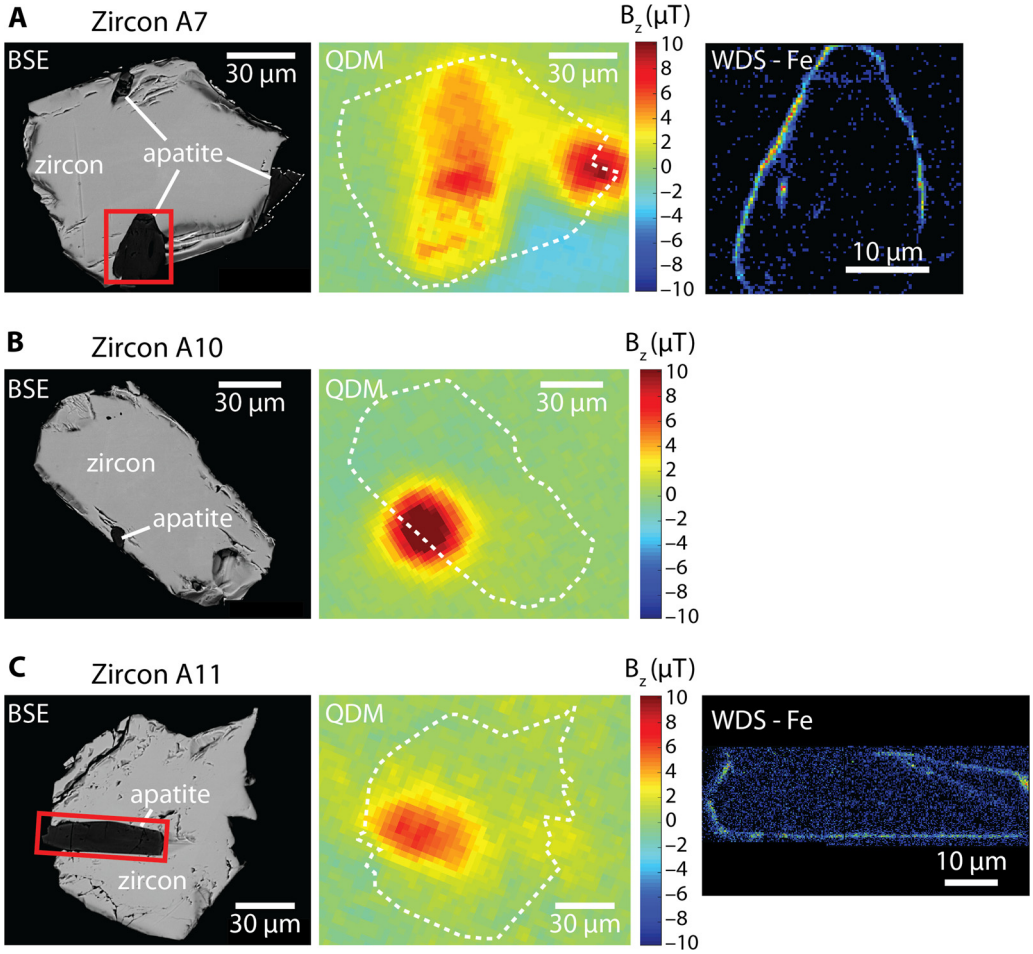

Fig. 6. Backscatter electron (BSE), quantum diamond microscope (QDM), and wavelength dispersion spectroscopy Fe element (WDS-Fe) maps of zircons showing the association of ferromagnetic sources with apatite inclusions. QDM maps were taken after a near-saturation IRM of 0.4 T was imparted in the out-of-plane (positive z) direction. Fields of view of WDS-Fe maps in panels A and C correspond to the red boxes in the BSE maps. Lighter colors reflect higher abundance of Fe in the WDS-Fe maps. (For interpretation of the references to color in this figure legend, the reader is referred to the web version of this article.)

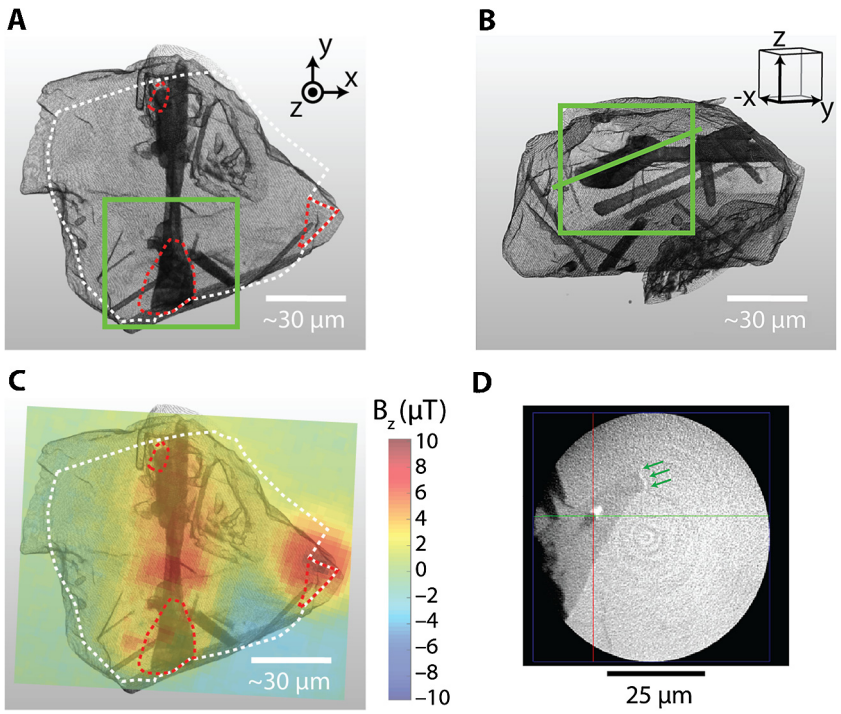

Fig. 7. High-resolution X-ray tomography. (**A**, **B**) Three-dimensional renderings of zircon A7 in two different perspectives and (**C**) comparison to magnetic field map from QDM. Dashed white line in panels (A) and (C) approximate the location of the BSE-imaged surface in Fig. 6, while dashed red lines highlight the locations of surface apatite as identified from BSE and WDS analysis. Comparison to BSE and WDS maps indicate that light gray in 3D renderings represents zircon while dark gray represents apatite inclusions. Because the BSE maps are limited to the exposed surface, differences in perspective, and loss of material during remounting of zircon for X-ray tomography (including detachment of the rightmost apatite inclusion), the outline of the zircon from the BSE map does not match exactly that from the X-ray tomographic renderings. Note the correspondence between the distribution of strong magnetization and internal, columnar apatite inclusions in panel (C). An animation of the 3D rendering is available in the Supplementary Data. (**D**) A slice taken from high resolution X-ray tomography scan using the Zeiss Xradia Ultra 800. The field of view in panel D is highlighted by green boxes in panels A and B, with the image taken parallel to the green diagonal in B. Spatially correlated with the buried magnetic feature in the QDM image is a 2 μm Fe-oxide particle (bright white feature) appearing as an inclusion in the apatite (dark gray). Possible smaller Fe-oxide particles are highlighted with green arrows in panel D. (For interpretation of the references to color in this figure, the reader is referred to the web version of this article.)

NRM moments of $\sim 1 \times 10^{-12}$ A m^2 and that the majority of zircon ferromagnetism is concentrated in localized regions of the zircon grain.

We further note that the SQUID microscope measures a peak field of 12 nT for zircon A15 at a sensor-to-sample distance of 180 μm. Assuming that remanence in zircon A15 is dominated by dispersed magnetization, we would expect the QDM map to show a signal with ~2.0 μT peak field centered on the zircon. This value is well above the field detection threshold of the QDM (Supplementary Materials). Therefore, the complete absence of such a signal from the QDM map confirms that any dispersed magnetization cannot constitute a significant fraction of the observed remanence.

To characterize the localized sources of remanent magnetization, we overlaid the QDM magnetic field maps on backscatter electron (BSE) images of the zircons with a registration accuracy of better than 10 μm. The comparison of QDM magnetic field and BSE images shows that the carriers of remanent magnetization are strongly associated with inclusions of apatite (Fig. 6). Wavelength dispersion spectroscopy (WDS) element mapping of Fe distribution confirms that Fe-bearing material occurs within and around apatite inclusions. Due to the higher saturation magnetization of magnetite and maghemite, only a volume equivalent to a 3.5 μm cube existing as single domain (SD) grains is needed to account for the $\sim 10^{-11}$ A m^2 IRM moment of typical zircons. This volume is consistent with that observed for Fe-bearing phases (Fig. 6). On the other hand, titanohematite requires volume equivalent to a 20 μm cube, which may be inconsistent with the WDS-Fe maps of zircons A7 and A11. The distribution of Fe-oxides shown in these zircons therefore likely represents that of magnetite or maghemite. However, we cannot rule out the presence of titanohematite in the subsurface of these zircons or in other zircons. We do not observe any magnetic sources associated with the outer surface of zircons apart from apatite inclusions, indicating that our zircons are not affected by oxide coatings. This difference between our samples and those of Sato et al. (2015) suggests that detrital zircons, such as those used in the latter study and those of the Jack Hills, are more susceptible to acquiring surface oxides.

We performed 3D X-ray tomography on zircon A7 to compare the observed magnetic fields with the internal distribution of accessory phases such as apatite within the zircon. We chose zircon A7 in part due to the presence of a strong magnetic signal detected by the QDM that does not correspond to any surface inclusions imaged by the electron microprobe (Fig. 6A), which suggests the presence of interior ferromagnetic phases. X-ray tomography of this sample indeed shows a group of apatite inclusions that correspond closely to the magnetic field source (Fig. 7A–C; Supplementary Data).

Subsequent higher magnification scans using the nanoscale XRM of a 50 μm region (green box in Fig. 7A, B) reveal the presence of high X-ray absorption grains (candidate Fe-oxides) both within the apatite inclusion and at the boundary between the apatite and its zircon host (Fig. 7D). To summarize the results of zircon microscopy, a combination of surface BSE and WDS mapping and 3D X-ray tomography shows that all magnetic signals observed using the QDM correspond to exposed or interior apatite inclusions.

4. Discussion

Our paleomagnetic measurement of 30 Bishop Tuff zircons showed that all specimens carry resolvable remanent magnetization with NRM intensities between 5×10^{-14} and 6×10^{-12} A m^2.

Thermal demagnetization and dual-heating paleointensity experiments on 18 zircons indicate that, once filtered using several reliability criteria, approximately half of individual zircons are capable of accurately recording a primary geomagnetic field with 1σ uncertainties of less than 6.8 μT. The agreement between our single zircon paleointensities and those inferred from bulk samples demonstrates the lack of contamination during our analysis procedures. The apparent ubiquity of ferromagnetic inclusions in zircon capable of carrying paleomagnetic information suggests that, given adequate preservation, single zircon crystals are a potentially robust source of constraints on ancient magnetic fields.

Our microscopy of Bishop Tuff zircons shows that ferromagnetic minerals are exclusively associated with apatite, which is the most common inclusion found in zircon crystals (Jennings et al., 2011). Embedded, euhedral grains of apatite similar to those observed in our Bishop Tuff zircons have been observed in zircons extracted from a wide range of whole rock compositions (Corfu et al., 2003). Furthermore, titanomagnetites in silica-rich magmas may crystallize at temperatures as high as ∼1100 °C and continue to form over a wide range of temperatures (Ghiorso and Sack, 1991). In comparison, apatite saturates over a lower range of temperatures between 700 and 900 °C for similar melts (Harrison and Watson, 1984), permitting the inclusion of early-formed titanomagnetites in apatite. As expected for the host phase, zircon in the Bishop Tuff continued to crystallize at temperatures as low as ∼720 °C (Reid et al., 2011). Therefore, the localization of such ferromagnetic grains in included apatites as observed in the Bishop Tuff zircons may be common in silicic, zircon-bearing rocks, leading to a broadly applicable mineralogical criterion for the preservation of primary remanent magnetization in ancient zircons. In this case, the potential of a given population of zircons to retain a primary paleomagnetic record would depend strongly on the preservation of primary apatite inclusions.

Because apatite is susceptible to dissolution and replacement by aqueous fluids (Nutman et al., 2014), ancient zircons that have undergone metasomatism may not retain a primary paleomagnetic record. In the case of the Jack Hills zircons, comparison to modern zircons from similar crystallization environments suggests that approximately 90% of apatite inclusions have been removed during secondary metasomatic events (Rasmussen et al., 2011). However, although only ∼5% of Jack Hills zircons are observed with apatite inclusions, none of these inclusions are adjacent to cracks and thereby show no evidence for a secondary origin (Bell et al., 2015; Yamamoto et al., 2013). At the same time, electron microscopy of ∼3.3 Ga Jack Hills zircons has revealed Fe-oxide, in the form of hematite, precipitated during secondary alteration in highly damaged zones (Utsunomiya et al., 2007), while only ∼7% of visible iron oxides are no associated with cracks or annealed cracks (Bell et al., 2015).

Synthesizing these observations with our results, primary remanent magnetization is potentially retained in select sub-volumes of Jack Hills zircons with unaltered apatite inclusions. However, given the rarity of apatite inclusions and the known presence of secondary iron oxides, careful attention, including high-resolution magnetic microscopy, must be devoted to establishing the locations and the primary nature of ferromagnetic inclusions before any primary record of the Earth's early magnetic field can be accepted as robust.

5. Conclusion

Using the SQUID microscope and a new measurement protocol with a noise floor of $\sim 6 \times 10^{-15}$ A m^2 in magnetic moment, we demonstrate that all 30 measured zircons extracted from the Bishop Tuff contain ferromagnetic inclusions that retain robustly recoverable remanent magnetization. Thermal demagnetization and paleointensity experiments on 18 zircons yielded eleven specimens that pass a set of reliability criteria based on the fraction of NRM used to derive paleointensity, the observed scatter in the best-fit paleointensity, and the degree of alteration during laboratory heating. The mean paleointensities derived from these zircons is 54.2 ± 6.8 μT, while a value of 42.6 ± 5.3 μT is obtained after excluding possible maghemite-bearing zircons. Both results are in agreement with the paleointensity of 43.0 ± 3.2 μT derived from high-fidelity bulk samples of the Bishop Tuff (Gee et al., 2010). AF demagnetization and IRM normalization paleointensity experiments on 15 zircons showed a higher degree of scatter than thermally demagnetized samples and suggest an inherently high ratio of NRM to near-saturation IRM corresponding to 0.17 in an ambient field of 50 μT. Magnetic microscopy using the QDM, combined with electron microscopy and X-ray tomography, showed that all detectable sources of ferromagnetism in Bishop Tuff zircons are hosted within or around apatite inclusions while typically $<1\%$ is likely carried by ferromagnetic grains uniformly dispersed within the zircon itself.

These results suggest that thermal demagnetization and paleointensity experiments on zircons may yield reliable estimates of ancient geomagnetic field intensities. However, the retention of primary paleomagnetic information is contingent on the preservation of zircon inclusions, most importantly of apatite. Paleomagnetic studies of single zircon grains, including the Jack Hills zircons (Tarduno et al., 2015), must therefore establish the primary nature of the ferromagnetic carriers before a robust characterization of ancient magnetic fields is possible. Micrometer-resolution magnetic imaging using the QDM, combined with electron and X-ray imaging technique, can play a critical role in identifying the ferromagnetic remanence carriers in other zircon populations and geological samples.

Acknowledgements

We thank Samuel A. Bowring, Timothy L. Grove, T. Mark Harrison, Dennis V. Kent, Simon Lock, and Joseph G. O'Rourke for insight and discussions that improved the content of this contribution. We also thank Eric Barry, Andrew Gregovich, and Jahandar Ramezani for zircon preparation, Nilanjan Chatterjee for electron microprobe assistance, Chenchen Luo for help with the QDM measurements, and Simon Doe and Christopher Bassell for arranging access to the XRM instrumentation at the ANFF SA node. RRF is supported by the Lamont-Doherty Post-Doctoral Fellowship. BPW, EAL, and JFDFA acknowledge support from NSF grant DMS-1521765. PK acknowledges support from the IC Postdoctoral Research Fellowship Program. DRG and RLW acknowledge support from the DARPA QuASAR HR0011-11-C-0073 and NSF EPMD 1408075 programs. JFE and RJH acknowledge funding under ERC Advance grant 320750—Nanopaleomagnetism. This work was performed (in part) at the South Australian node of the Australian National Fabrication Facility under the National Collaborative Research Infrastructure Strategy to provide nano and microfabrication facilities for Australia's researchers. We thank two anonymous reviewers for their helpful comments.

Appendix A. Supplementary material

Supplementary material related to this article can be found online at http://dx.doi.org/10.1016/j.epsl.2016.09.038.

References

Anderson, A.T., Newman, S., Williams, S.N., Druitt, T.H., Skirius, C., Stolper, E., 1989. H_2O, CO_2, Cl, and gas in Plinian and ash-flow Bishop Rhyolite. Geology 17, 221–225.

Bell, E.A., Boehnke, P., Hopkins-Wielicki, M.D., Harrison, T.M., 2015. Distinguishing primary and secondary inclusion assemblages in Jack Hills zircons. Lithos 234–235, 15–26. http://dx.doi.org/10.1016/j.lithos.2015.07.014.

Berndt, T., Muxworthy, A.R., Fabian, K., 2016. Does size matter? Statistical limits of paleomagnetic field reconstruction from small rock specimens. J. Geophys. Res., Solid Earth 121, 15–26.

Biggin, A.J., de Wit, M.J., Langereis, C.G., Zegers, T.E., Voute, S., Dekkers, M.J., Drost, K., 2011. Palaeomagnetism of Archaean rocks of the Onverwacht Group, Barberton Greenstone Belt (southern Africa): evidence for a stable and potentially reversing geomagnetic field at ca. 3.5 Ga. Earth Planet. Sci. Lett. 302, 314–328.

Bindeman, I.N., Valley, J.W., 2002. Oxygen isotope study of the Long Valley magma system, California: isotope thermometry and convection in large silicic magma bodies. Contrib. Mineral. Petrol. 144, 185–205.

Coe, R.S., Grommé, S., Mankinen, E.A., 1978. Geomagnetic paleointensities from radiocarbon-dated lava flows on Hawaii and the question of the Pacific nondipole low. J. Geophys. Res. 83, 1740–1756.

Corfu, F., Hanchar, J.M., Hoskin, P.W.O., Kinny, P., 2003. Atlas of zircon textures. Rev. Mineral. Geochem. 51, 469–500.

Crowley, J.L., Schoene, B., Bowring, S.A., 2007. U–Pb dating of zircon in the Bishop Tuff at the millennial scale. Geology 35, 1123–1126.

Darling, J., Storey, C., Hawkesworth, C.J., 2009. Impact melt sheet zircons and their implications for the Hadean crust. Geology 37, 927–930.

Dunlop, D.J., Ozdemir, O., 1997. Rock Magnetism: Fundamentals and Frontiers, Cambridge Studies in Magnetism. Cambridge University Press, New York.

Elkins-Tanton, L.T., Zaranek, S.E., Parmentier, E.M., Hess, P.C., 2005. Early magnetic field and magmatic activity on Mars from magma ocean cumulate overturn. Earth Planet. Sci. Lett. 236, 1–12.

Fabian, K., 2009. Thermochemical remanence acquisition in single-domain particle ensembles: a case for possible overestimation of the geomagnetic paleointensity. Geochem. Geophys. Geosyst. 10. http://dx.doi.org/10.1029/2009GC002420.

Froude, D.O., Ireland, T.R., Kinny, P.D., Williams, I.S., Compston, W., Williams, I.R., Myers, J.S., 1983. Ion microprobe identification of 4100–4200 Myr old terrestrial zircons. Nature 304, 616–618.

Fu, R.R., Lima, E.A., Weiss, B.P., 2014a. No nebular magnetization in the Allende CV carbonaceous chondrite. Earth Planet. Sci. Lett. 404, 54–66.

Fu, R.R., Weiss, B.P., Lima, E.A., Harrison, R.J., Bai, X.-N., Desch, S.J., Ebel, D.S., Suavet, C., Wang, H., Glenn, D., Le Sage, D., Kasama, T., Walsworth, R.L., Kuan, A.T., 2014b. Solar nebula magnetic fields recorded in the Semarkona meteorite. Science 346, 1089–1092.

Gee, J.S., Yu, Y., Bowles, J., 2010. Paleointensity estimates from ignimbrites: an evaluation of the Bishop Tuff. Geochem. Geophys. Geosyst. 11, 3.

Ghiorso, M.S., Sack, R.O., 1991. Fe–Ti oxide geothermometry: thermodynamic formulation and the estimation of intensive variables in silicic magmas. Contrib. Mineral. Petrol. 108, 485–510.

Glenn, D.R., Lee, K., Park, H., Weissleder, R., Yacoby, A., Lukin, M.D., Lee, H., Walsworth, R.L., Connolly, C.B., 2015. Single-cell magnetic imaging using a quantum diamond microscope. Nat. Methods 12, 736–738.

Hale, C.J., 1987. The intensity of the geomagnetic field at 3.5 Ga – paleointensity results from the Komati Formation, Barberton Mountain Land, South Africa. Earth Planet. Sci. Lett. 86, 354–364.

Hale, C.J., Dunlop, D.J., 1984. Evidence for an early Archean geomagnetic field: a paleomagnetic study of the Komati Formation, Barberton greenstone belt, South Africa. Geophys. Res. Lett. 11, 97–100.

Harrison, T.M., 2009. The Hadean crust: evidence from >4 Ga zircons. Annu. Rev. Earth Planet. Sci. 37, 479–505.

Harrison, T.M., Watson, E.B., 1984. The behavior of apatite during crustal anatexis: equilibrium and kinetic considerations. Geochim. Cosmochim. Acta 48, 1467–1477.

Hildreth, W., 1979. The Bishop Tuff: evidence for the origin of compositional zonation in silicic magma chambers. Spec. Pap., Geol. Soc. Am. 180, 43–76.

Holt, E.W., Taylor, H.P., 1998. 18O/16O mapping and hydrogeology of a short-lived (10 years) fumarolic (>500 °C) meteoric–hydrothermal event in the upper part of the 0.76 Ma Bishop Tuff outflow sheet, California. J. Volcanol. Geotherm. Res. 83, 115–139.

Hopkins, M.D., Harrison, T.M., E, M.C., 2010. Constraints on Hadean geodynamics from mineral inclusions in N4 Ga zircons. Earth Planet. Sci. Lett. 298, 367–376.

Jennings, E.S., Marschall, H.R., Hawkesworth, C.J., Storey, C.D., 2011. Characterization of magma from inclusions in zircon: apatite and biotite work well, feldspar less so. Geology 39, 863–866. http://dx.doi.org/10.1130/G32037.1.

Kemp, A.I.S., Wilde, S.A., Hawkesworth, C.J., Coath, C.D., Nemchin, A., Pidgeon, R.T., Vervoort, J.D., Dufrane, S.A., 2010. Hadean crustal evolution revisited: new constraints from Pb–Hf isotope systematics of the Jack Hills zircons. Earth Planet. Sci. Lett. 296, 45–56.

Kirschvink, J.L., 1980. The least-squares line and plane and the analysis of paleomagnetic data: examples from Siberia and Morocco. Geophys. J. R. Astron. Soc. 62, 699–718.

Kulikov, Y.N., Lammer, H., Lichtenegger, H.I.M., Penz, T., Breuer, D., Spohn, T., Lundin, R., Biernat, H., 2007. A comparative study of the influence of the active young sun on the early atmospheres of Earth, Venus, and Mars. Space Sci. Rev. 129, 207–243.

Labrosse, S., Hernlund, J.W., Coltice, N., 2007. A crystallizing dense magma ocean at the base of the Earth's mantle. Nature 450.

Lewis, R.R., Senftle, F.E., 1966. The source of ferromagnetism in zircon. Am. Mineral. 51, 1467–1475.

Lima, E.A., Weiss, B.P., 2016. Ultra-high sensitivity moment magnetometry of geological samples using magnetic microscopy. Geochem. Geophys. Geosyst. 17. http://dx.doi.org/10.1002/2016GC006487.

McElhinny, M.W., Senanayake, W.E., 1980. Paleomagnetic evidence for the existence of the geomagnetic field 3.5 Ga ago. J. Geophys. Res. 85, 3523–3528.

Mojzsis, S.J., Harrison, T.M., Pidgeon, R.T., 2001. Oxygen-isotope evidence from ancient zircons for liquid water at Earth's surface 4,300 Myr ago. Nature 409, 178–181.

Nimmo, F., Stevenson, D., 2000. Influence of early plate tectonics on the thermal evolution and magnetic field of Mars. J. Geophys. Res. 105, 11969–11979.

Nutman, A.P., 2006. Comment on "Zircon thermometer reveals minimum melting conditions on earliest Earth". Science 311, 779b.

Nutman, A.P., Maciejowski, R., Wan, Y., 2014. Protoliths of enigmatic Archaean gneisses established from zircon inclusion studies: case study of the Caozhuang quartzite, E. Hebei, China. Geosci. Front. 5, 445–455. http://dx.doi.org/10.1016/j.gsf.2013.10.001.

O'Neill, C., Debaille, V., 2014. The evolution of Hadean–Eoarchaean geodynamics. Earth Planet. Sci. Lett. 406, 49–58.

O'Rourke, J.G., Stevenson, D.J., 2016. Powering Earth's dynamo with magnesium precipitation from the core. Nature.

Ozima, M., Seki, K., Terada, N., Miura, Y.N., Podosek, F.A., Shinagawa, H., 2005. Terrestrial nitrogen and noble gases in lunar soils. Nature 436, 655–659.

Rasmussen, B., Fletcher, I.R., Muhling, J.R., Gregory, C.J., Wilde, S.A., 2011. Metamorphic replacement of mineral inclusions in detrital zircon from Jack Hills, Australia: implications for the Hadean Earth. Geology 39, 1143–1146.

Reid, M.R., Vazquez, J.A., Schmitt, A.K., 2011. Zircon-scale insights into the history of a Supervolcano, Bishop Tuff, Long Valley, California, with implications for the Ti-in-zircon geothermometer. Contrib. Mineral. Petrol. 161, 293–311.

Riehle, J.R., 1973. Calculated compaction profiles of rhyolitic ash-flow tuffs. Geol. Soc. Am. Bull. 84, 2193–2216.

Riehle, J.R., Miller, T.F., Bailey, R.A., 1995. Cooling, degassing and compaction of rhyolitic ash flow tufts: a computational model. Bull. Volcanol. 57, 319–336.

Riehle, J.R., Miller, T.F., Paquereau-Lebti, P., 2010. Compaction profiles of ash-flow tuffs: modeling versus reality. J. Volcanol. Geotherm. Res. 195, 106–120.

Sato, M., Yamamoto, S., Yamamoto, Y., Okada, Y., Ohno, M., Tsunakawa, H., Maruyama, S., 2015. Rock-magnetic properties of single zircon crystals sampled from the Tanzawa tonalitic pluton, central Japan. Earth Planets Space 67, 150.

Selkin, P.A., Tauxe, L., 2000. Long-term variations in palaeointensity. Philos. Trans. R. Soc. Lond. A 358, 1065–1088.

Singer, B.S., Hoffman, K.A., Coe, R.S., Brown, L.L., Jicha, B.R., Pringle, M.S., Chauvin, A., 2005. Structural and temporal requirements for geomagnetic field reversal deduced from lava flows. Nature 434, 633–636.

Snow, E., Yung, R.A., 1988. Origin of cryptoperthites in the Bishop Tuff and their bearing in its thermal history. J. Geophys. Res. 93, 8975–8984.

Tarduno, J.A., Cottrell, R.D., Davis, W.J., Nimmo, F., Bono, R.K., 2015. A Hadean to Paleoarchean geodynamo recorded by single zircon crystals. Science 349, 521–524.

Tarduno, J.A., Cottrell, R.D., Watkeys, M., Hofmann, A., Doubrovine, P.V., Mamajek, E.E., Liu, D., Sibeck, D.G., Neukirch, L.P., Usui, Y., 2010. Geodynamo, solar wind, and magnetopause 3.4 to 3.45 billion years ago. Science 327, 1238–1240.

Tauxe, L., Gee, J.S., Steiner, M.B., Staudigel, H., 2013. Paleointensity results from the Jurassic: new constraints from submarine basaltic glasses of ODP Site 801C. Geochem. Geophys. Geosyst. 14, 4718–4733.

Tauxe, L., Staudigel, H., 2004. Strength of the geomagnetic field in the Cretaceous Normal Superchron: new data from submarine basaltic glass of the Troodos Ophiolite. Geochem. Geophys. Geosyst. 5. http://dx.doi.org/10.1029/2003GC000635.

Timms, N.E., Reddy, S.M., Fitz Gerald, J.D., Green, L., Muhling, J.R., 2012. Inclusion-localised crystal-plasticity, dynamic porosity, and fast-diffusion pathway generation in zircon. J. Struct. Geol. 35, 78–89.

Utsunomiya, S., Valley, J.W., Cavosie, A.J., Wilde, S.A., Ewing, R.C., 2007. Radiation damage and alteration of zircon from a 3.3 Ga porphyritic granite from the Jack Hills, Western Australia. Chem. Geol. 236, 92–111. http://dx.doi.org/10.1016/j.chemgeo.2006.09.003.

Valley, J.W., Cavosie, A.J., Ushikubo, T., Reinhard, D.A., Lawrence, D.F., Larson, D.J., Clifton, P.H., Kelly, T.F., Wilde, S.A., Moser, D.E., Spicuzza, M.J., 2014. Hadean age for a post-magma-ocean zircon confirmed by atom-probe tomography. Nat. Geosci. 7, 219–223. http://dx.doi.org/10.1038/ngeo2075.

Wallace, P.J., Anderson, A.T., Davis, A.M., 1999. Gradients in H_2O, CO_2, and exsolved gas in a large-volume silicic magma system: interpreting the record preserved in melt inclusions from the Bishop Tuff. J. Geophys. Res. 104 (20), 0997. p. 122.

Watson, E.B., Harrison, T.M., 2005. Zircon thermometer reveals minimum melting conditions on earliest Earth. Science 308, 841–844.

Weiss, B.P., Lima, E.A., Fong, L.E., Baudenbacher, F.J., 2007. Paleomagnetic analysis using SQUID microscopy. J. Geophys. Res. 112, B09105. http://dx.doi.org/10.1029/2007JB004940.

Weiss, B.P., Maloof, A.C., Tailby, N., Ramezani, J., Fu, R.R., Hanus, V., Trail, D., Watson, E.B., Harrison, T.M., Bowring, S.A., Kirschvink, J.L., Swanson-Hysell, N.L., Coe, R.S., 2015. Pervasive remagnetization of detrital zircon host rocks in the Jack Hills, Western Australia and implications for records of the early geodynamo. Earth Planet. Sci. Lett. 430, 115–128.

Wilde, S.A., Valley, J.W., Peck, W.H., Graham, C.M., 2001. Evidence from detrital zircons for the existence of continental crust and oceans on the Earth 4.4 Gyr ago. Nature 409, 175–178.

Wilson, C.J.N., Hildreth, W., 1997. The Bishop Tuff: new insights from eruptive stratigraphy. J. Geol. 105, 407–439.

Wilson, C.J.N., Hildreth, W., 2003. Assembling an ignimbrite: mechanical and thermal building blocks in the Bishop Tuff, California. J. Geol. 111, 653–670.

Yamamoto, S., Komiya, T., Shimojo, M., Sakata, S., Maki, K., Hirata, T., 2013. Apatite inclusions in Hadean zircon from Jack Hills, Australia. In: Goldschmidt Conf. Abs., p. 2541.

Yoshihara, A., Hamano, Y., 2004. Paleomagnetic constraints on the Archean geomagnetic field intensity obtained from komatiites of the Barberton and Belingwe greenstone belts, South Africa and Zimbabwe. Precambrian Res. 131, 111–142.

Yu, Y., 2011. Importance of cooling rate dependence of thermoremanence in paleointensity determination. J. Geophys. Res. 116, B09101.

Yu, Y., Tauxe, L., Genevey, A., 2004. Toward an optimal geomagnetic field intensity determination technique. Geochem. Geophys. Geosyst. 5. http://dx.doi.org/10.1029/2003GC000630.

Supplementary Materials for:

Evaluating the paleomagnetic potential of single zircon crystals using the Bishop Tuff

Roger R. Fu, Benjamin P. Weiss, Eduardo A. Lima, Pauli Kehayias, Jefferson F. D. F. Araujo, David Glenn, Jeff Gelb, Joshua F. Einsle, Ann M. Bauer, Richard J. Harrison, Guleed A.H. Ali, Ronald L. Walsworth

AF demagnetization of zircon

We performed AF demagnetization of NRM followed by AF demagnetization of IRM on 15 zircons. The close (1.5 mm) separation of the zircons on the epoxy holder resulted in contaminated field signals for three zircons mounted adjacent to much stronger samples. As such, reliable magnetic moment inversions were recovered from 12 of the 15 zircons. For these, initial NRM intensities range between 1.9×10^{-13} and 6.2×10^{-12} Am^2 with a mean of 2.3×10^{-12} Am^2. AF application yielded significantly noisier demagnetization sequences compared to thermal demagnetization (Fig. 2F). We applied AF in 5 mT steps up to 20 mT and in 10 mT steps between 20 and 140 mT. All AF demagnetization sequences showed one identifiable component of magnetization that is fully removed by AF application of between 70 and 130 mT. To derive paleointensities using the IRM normalization method, we imparted a near-saturation IRM of 0.4 T and conducted AF demagnetization using the same steps as described above up to 90 mT. We then computed the least-squares best-fit line to a diagram of NRM remaining and IRM removed to find the ratio of NRM to IRM in the 0 to 90 mT range (Fig. 4F; Table S1).

The mean NRM to near-saturation IRM ratio (*NRM*/*IRM*) for 12 zircons is 0.15, which may be converted to a paleointensity (B_{paleo}) estimate using the relationship:

$$B_{paleo} = a(NRM/IRM)$$

where a is an empirically calibrated factor. Adopting a = 3000 μT based on experiments on magnetite and titanomagnetite with a wide range of domain states (Gattacceca and Rochette, 2004; Kletetschka et al., 2003), we derive a paleointensity of 437 ± 95 μT (1σ), which is larger than the expected value by a factor of 10 (Gee et al., 2010). This result implies that Bishop Tuff zircons have anomalously low values of $a \cong$ 300 μT, which corresponds to *NRM*/*IRM* ≅ 0.17 for a TRM acquired in an ambient field of 50 μT. For zircons with similar ferromagnetic mineralogy and magnetization mechanism as those analyzed in this study, we recommend a calibration factor of 300 μT, which is expected to yield 1σ errors on the order of 22% compared to the 13% from dual heating experiments.

The value of a = 530 inferred by Kletetschka et al., (2004) for hematite represents a closer match to our inferred value, although we favor magnetite or maghemite as the dominant ferromagnetic phase in most of our zircons. At the same time, our values of *NRM*/*IRM* are broadly consistent with the range (0.01 to 1) observed in Tanzawa pluton zircons (Sato et al., 2015). Similarly high values of *NRM/IRM* have been observed in natural single-domain magnetite particles embedded in anorthosite (Kletetschka et al., 2006). At the same time, although observed *NRM*/*IRM* values in synthetic magnetite-bearing samples are lower by at least 40% compared to our results, grain sizes in the 100 nm to 1 μm range represent the closest

approximation (Yu, 2006). These small inferred grain sizes are consistent with our results from electron microscopy.

Discussion of methodology for constraining the dispersed zircon magnetization

As described in Section 3.2 we use high-resolution QDM maps of the magnetic field from a zircon (A15) magnetized in a near-saturation 0.4 T magnetic field to constrain the possible moment contribution from volumetrically dispersed ferromagnetic sources in the zircon [e.g., Timms et al., (2012)]. Here we discuss the uncertainties of this analysis and argue that it is sufficient to produce a reliable, conservative upper bound on the intensity of dispersed magnetization. To map between the dispersed magnetization and the imaged magnetic field, we approximated the zircon as a uniformly magnetized sphere with a 40 μm radius. Because the external magnetic field of a uniformly magnetized sphere is equivalent to that of a dipolar source situated at its center (Dunlop and Ozdemir, 1997), we generate a magnetic field map for a given dispersed magnetization intensity assuming that a dipole source is situated at the center of the zircon at 40 μm depth (Fig. S1C). The minimal amount of polishing conducted for the epoxy-mounted zircons resulted in the removal of only a small fraction of the total volume, resulting in sub-equant zircons that have aspect ratios rarely greater than 2:1 (Fig. 7). Even so, modeling the zircon as a uniformly magnetized sphere is an approximation. Furthermore, the subtraction of the fitted localized sources assumes that these are well-modeled by a dipole; therefore, any non-dipolarity of the actual localized sources would result in the incomplete or excessive subtraction of the signals. A more comprehensive analysis would study the magnetic field from a zircon with no localized sources, avoiding any uncertainties introduced by the subtraction of localized sources. Furthermore, the QDM image in Fig. 6 has a field gradient from the applied magnetic

field required by the QDM measurement with a full range of 0.46 μT across the image. Subtracting this gradient leaves a uniform background field and yields a weaker value for the dispersed zircon dipole moment. However, such a subtraction may also remove some field contribution from the dispersed magnetization, leading to an overly stringent limit. We chose the more conservative approach and refrain from subtracting the background gradient, strengthening the assertion that ~1% is an upper bound for the contribution of the dispersed magnetization to the total zircon moment. Future analyses can more accurately constrain the dispersed magnetization by modeling realistic zircon geometries, studying zircons with no localized sources near the surface, improving the QDM applied magnetic field gradient, and distinguishing localized and dispersed sources by successively polishing or raising the diamond sensor height in 10 μm steps.

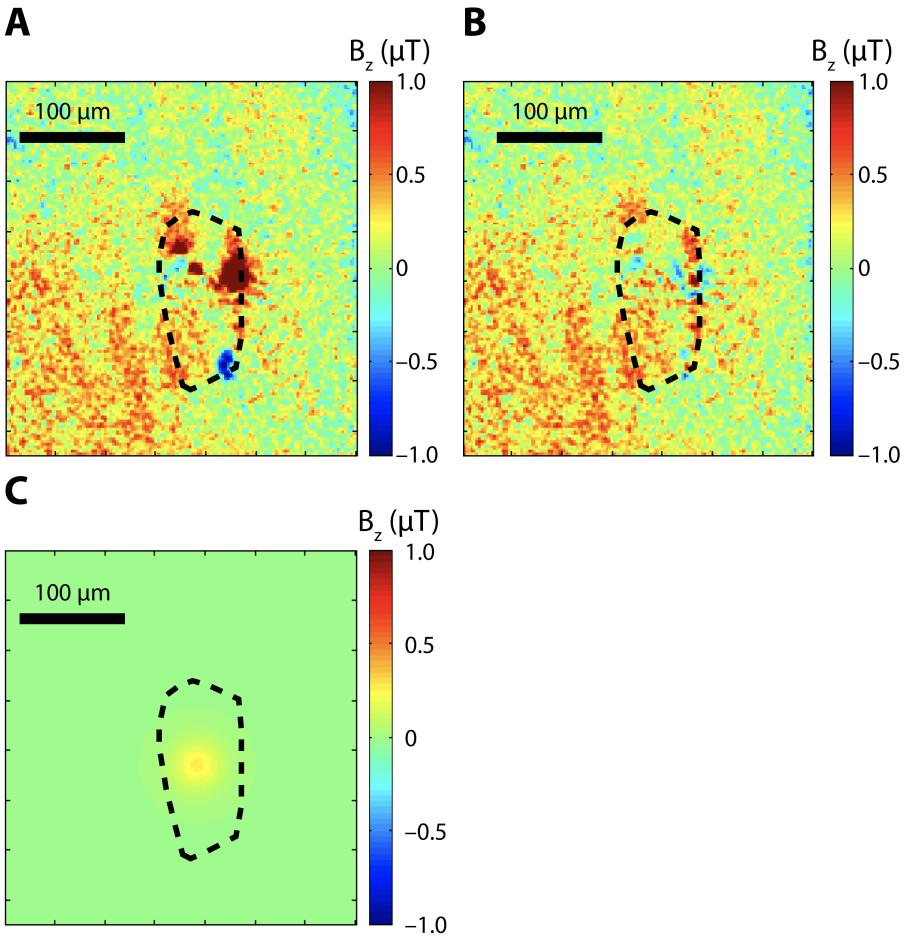

Figure S1: Elimination of localized ferromagnetic source signals and inversion for the maximum dispersed magnetization moment of zircon A15, which has been given a 0.4 T near-saturation IRM in the out-of-plane direction. (**A**) Raw QDM image of the out-of-plane magnetic field component where the dashed black line denotes the outline of the zircons. (**B**) Processed QDM image where the four strongest localized magnetic moment sources have been fitted assuming a dipole source and removed. (**C**) Magnetic field corresponding to the best-fit dipole moment source for the map in panel (B) assuming source location at the center of the zircon and 40 μm depth. This magnetic field distribution fails to reproduce the pattern shown in panel B, strongly suggesting that volumetrically dispersed ferromagnetic grains are not a significant contributor to the total magnetization.

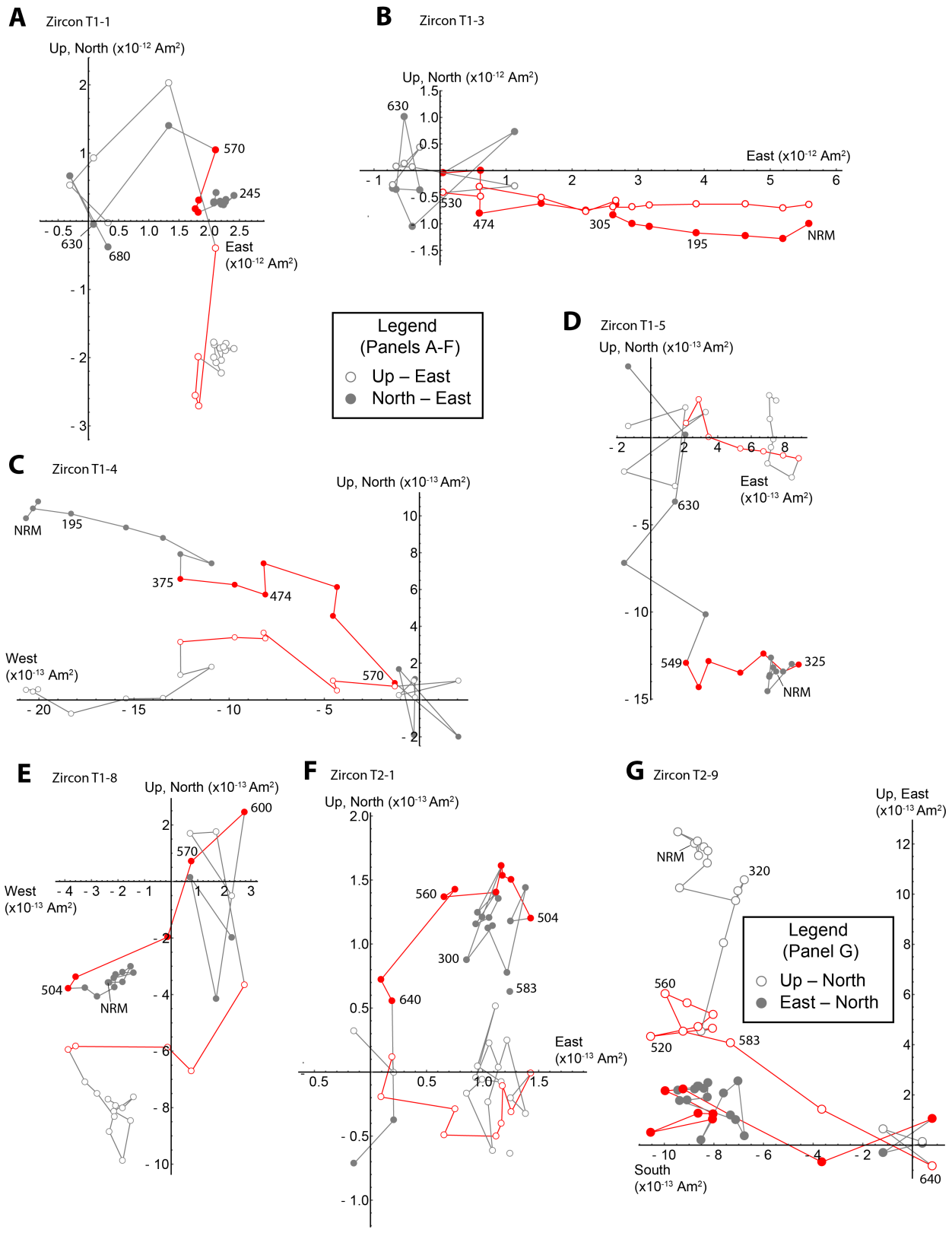
A
Zircon T1-1
Up, North (x10-12 Am2)
East (x10-12 Am2)
570
245
630
680
B
Zircon T1-3
Up, North (x10-12 Am2)
East (x10-12 Am2)
630
530
474
305
195
NRM
Legend (Panels A-F)
Up – East
North – East
C
Zircon T1-4
Up, North (x10-13 Am2)
West (x10-13 Am2)
NRM
195
375
474
570
D
Zircon T1-5
Up, North (x10-13 Am2)
East (x10-13 Am2)
630
549
325
NRM
E
Zircon T1-8
Up, North (x10-13 Am2)
West (x10-13 Am2)
600
570
504
NRM
F
Zircon T2-1
Up, North (x10-13 Am2)
East (x10-13 Am2)
560
504
300
583
640
G
Zircon T2-9
Up, East (x10-13 Am2)
South (x10-13 Am2)
NRM
320
560
520
583
640
Legend (Panel G)
Up – North
East – North

Figure S2: Orthogonal projection diagrams of thermal demagnetization sequences for all zircons passing the quality criteria and included in the calculation of the final mean paleointensity. Zircons already shown in Fig. 2 are excluded here. Solid and open circles denote the projection of magnetization onto the north-east and up-east planes, respectively. Red data points indicate range used in paleointensity calculations. Paleointensity (Arai) diagrams for the zircons shown here are plotted in Fig. S3.

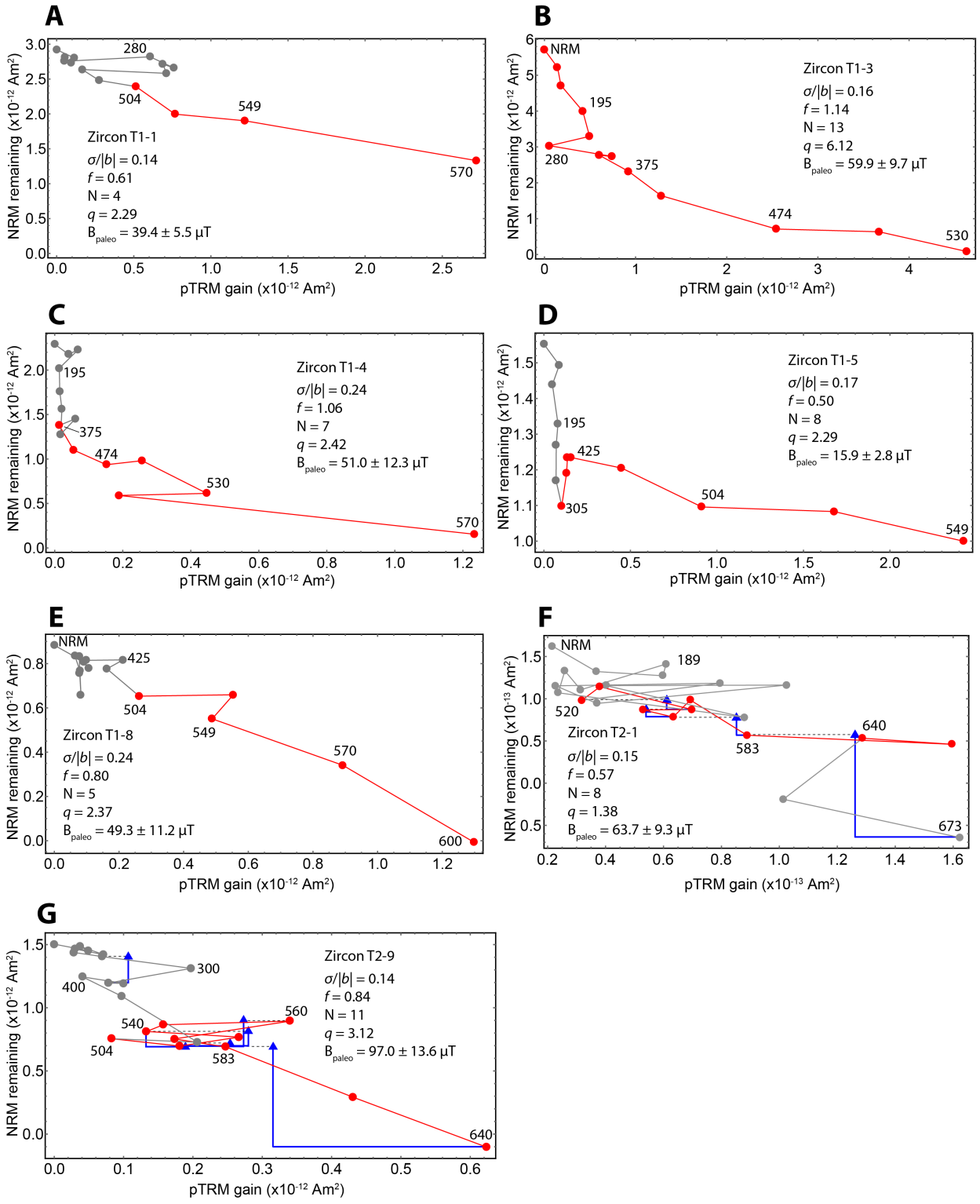

Figure S3: Paleointensity (Arai) diagrams for all thermally demagnetized zircons passing the quality criteria and included in the calculation of the final mean paleointensity. Zircons already

shown in Fig. 4 are excluded here. Directional demagnetization data (Zijderveld diagrams) for these zircons are shown in Fig. S2. Zircons in the T1 group were treated with sequential thermal demagnetization and pTRM acquisition while those in the T2 group were measured using the IZZI Thellier-Thellier protocol including pTRM checks (blue triangles). The data ranges chosen for computing the paleointensity are indicated in red.

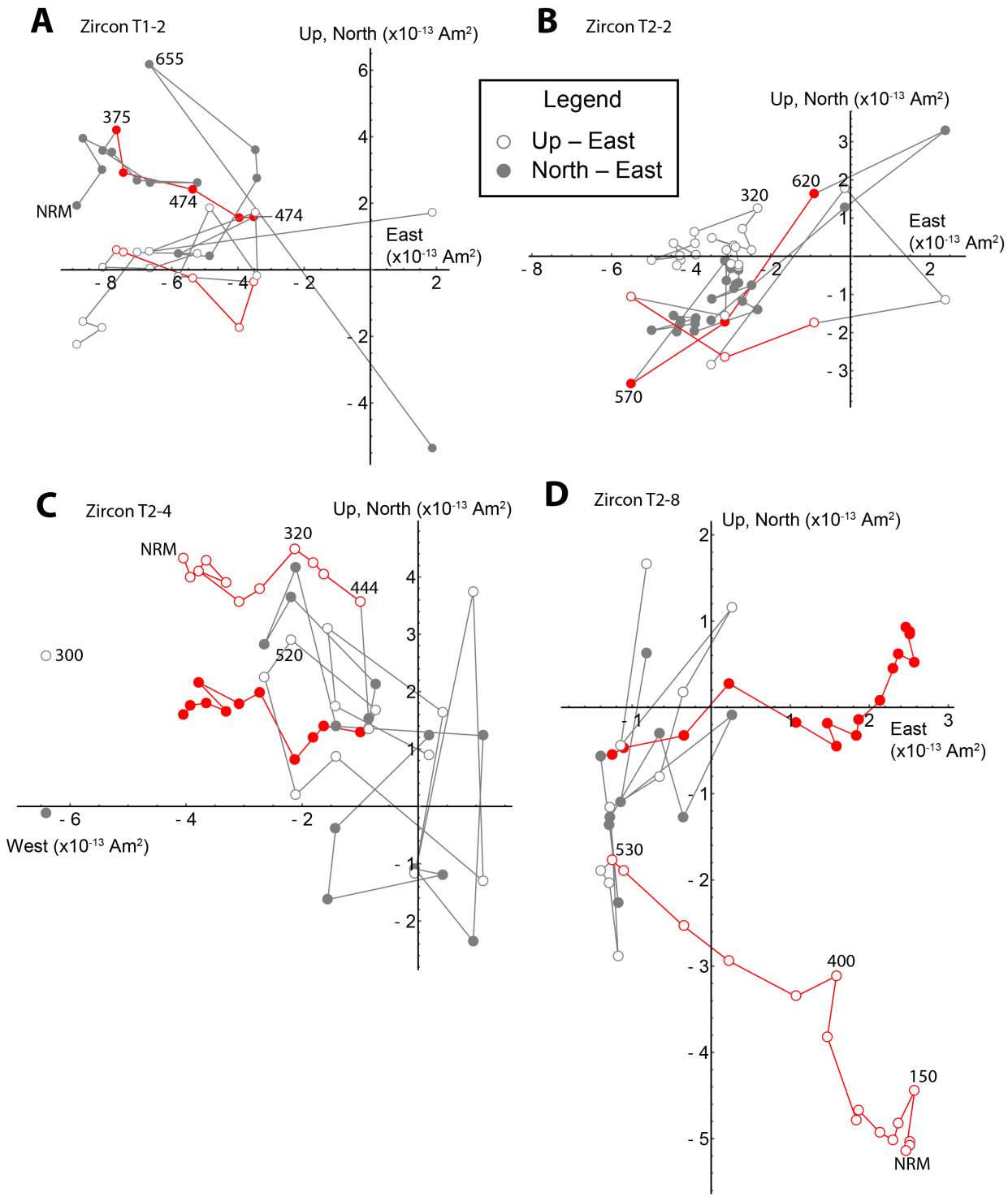

Figure S4: Orthogonal projection diagrams of demagnetization sequences for all zircons failing the quality criteria and not included in the calculation of the final mean paleointensity. Zircons already shown in Fig. 2 are excluded here. Solid and open circles denote the projection of

magnetization onto the north-east and up-east planes, respectively. Red data points indicate range used in paleointensity calculations. Paleointensity (Arai) diagrams for the zircons shown here are plotted in Fig. S5.

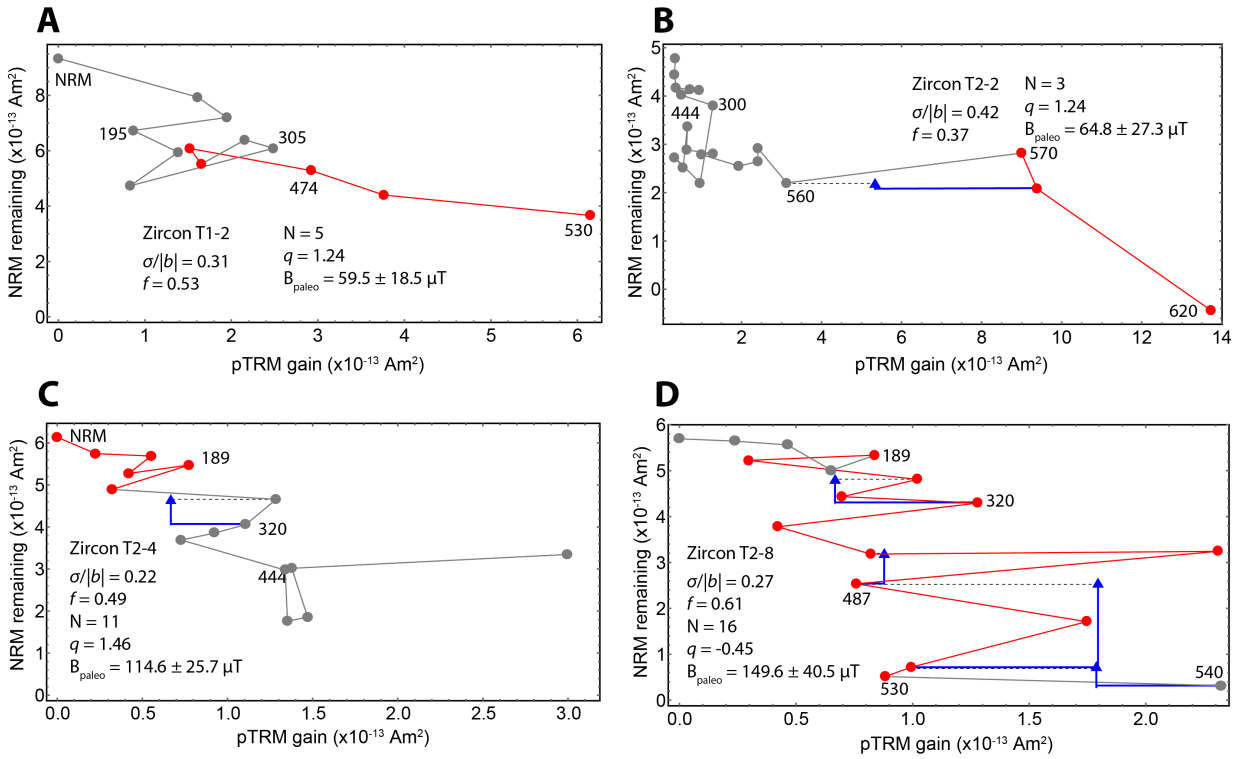

Figure S5: Paleointensity (Arai) diagrams for all thermally demagnetized zircons failing the quality criteria and not included in the calculation of final mean paleointensity. Zircons already shown in Fig. 4 are excluded here. Directional demagnetization data (Zijderveld diagrams) for these zircons are shown in Fig. S4. Zircons in the T1 group were treated with sequential thermal demagnetization and pTRM acquisition while those in the T2 group were measured using the IZZI Thellier-Thellier protocol including pTRM checks (blue triangles). The data ranges chosen for computing paleointensity are indicated in red.

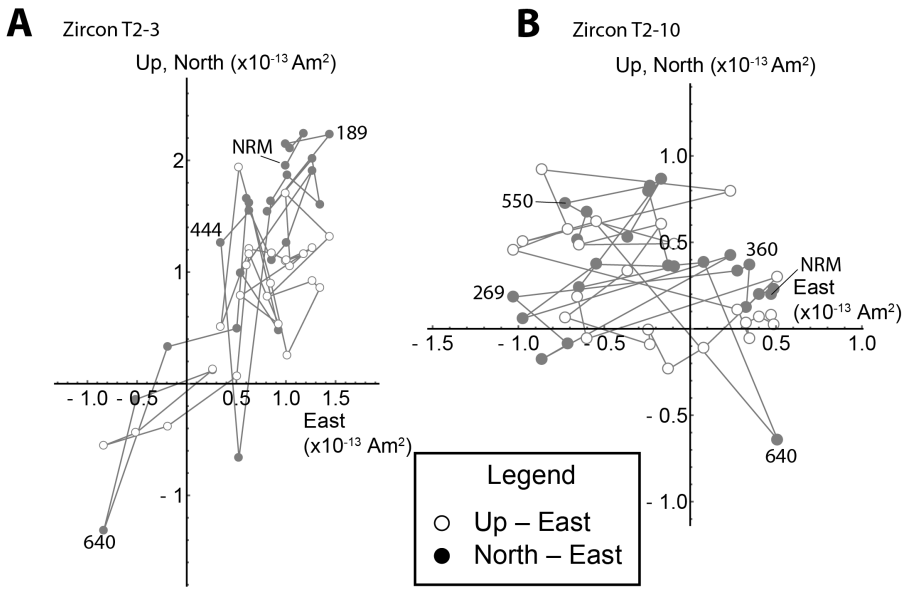

Figure S6: Orthogonal projection diagrams of demagnetization sequences for the two zircons with no components of magnetization analyzed for paleointensity. Note the very low magnetic moments compared to most other zircons. Solid and open circles denote the projection of magnetization onto the north-east and up-east planes, respectively.

Table S1: Results of AF demagnetization of single zircons and IRM paleointensity experiments

Sample name	MAD (°)	Normalized scatter ($\sigma/\|b\|$)	NRM/IRM	Paleointensity (μT)	1σ uncertainty (μT)
A1	29.1	0.18	0.28	826	146
A2	26.1	0.32	0.03	88.4	28
A3	22.1	0.21	0.16	465	99
A4	13.7	0.12	0.21	620	76
A5	44.8	0.22	0.08	236	51
A6	15.2	0.08	0.06	192	14
A7	26.1	0.31	0.11	335	103
A8	22.3	0.20	0.10	289	58
A9	20.5	0.15	0.31	915	135
A10	30.2	0.15	0.27	819	126
A11	30.4	N/A	N/A	N/A	N/A
A12	33.2	2.57	0.01	22.4	57.7
Mean			0.15	437	94.7

Notes: Due to zircon A11's close location to the much stronger zircon A12 on the sample mount, we were unable to recover a reliable IRM demagnetization sequence. For the same reason, we were unable to recover reliable NRM or IRM data from three further zircons (A13-A15), which are not listed here. AF range fitted for the NRM to near-saturation IRM ratio (NRM/IRM) is 0 to 90 mT for all samples. The number of fitted steps is 12 for all samples. IRM paleointensities are computed using the slope of the standard least squares best fit line and an empirical factor of 3000 μT (Gattacceca and Rochette, 2004; Kletetschka et al., 2003). Column 2 gives the maximum angular deviation, which describes the scatter of demagnetization data around the best-fit direction. Column 3 gives the 1σ uncertainty of the best-fit slope in the Arai diagram normalized by the slope value.

References:

Dunlop, D.J., Ozdemir, O., 1997. Rock Magnetism: Fundamentals and Frontiers, Cambridge Studies in Magnetism. Cambridge University Press, New York.

Gattacceca, J., Rochette, P., 2004. Toward a robust normalized magnetic paleointensity method applied to meteorites. Earth Planet. Sci. Lett. 227, 377–393.

Gee, J.S., Yu, Y., Bowles, J., 2010. Paleointensity estimates from ignimbrites: An evaluation of the Bishop Tuff. Geochem. Geophys. Geosyst. 11, 3.

Kletetschka, G., Acuna, M.H., Kohout, T., Wasilewski, P.J., Connerney, J.E.P., 2004. An empirical scaling law for acquisition of thermoremanent magnetization. Earth Planet. Sci. Lett. 226, 521–528.

Kletetschka, G., Fuller, M.D., Kohout, T., Wasilewski, P.J., Herrero-Bervera, E., Ness, N.F., Acuna, M.H., 2006. TRM in low magnetic fields: a minimum field that can be recorded by large multidomain grains. Phys. Earth Planet. Inter. 154, 290–298.

Kletetschka, G., Kohout, T., Wasilewski, P.J., 2003. Magnetic remanence in the Murchison meteorite. Meteorit. Planet. Sci. 38, 399–405.

Sato, M., Yamamoto, S., Yamamoto, Y., Okada, Y., Ohno, M., Tsunakawa, H., Maruyama, S., 2015. Rock-magnetic properties of single zircon crystals sampled from the Tanzawa tonalitic pluton, central Japan. Earth Planets Sp. 67, 150.

Timms, N.E., Reddy, S.M., Fitz Gerald, J.D., Green, L., Muhling, J.R., 2012. Inclusion-localised crystal-plasticity, dynamic porosity, and fast-diffusion pathway generation in zircon. J. Struct. Geol. 35, 78–89.

Yu, Y.J., 2006. How accurately can NRM/SIRM determine the ancient planetary magnetic field intensity? Earth Planet. Sci. Lett. 250, 27–37.